Assessment of the z˜ time-filtered Arbitrary Lagrangian-Eulerian coordinate in a global eddy-permitting ocean model

Alex Megann[1], Jérôme Chanut[2] and David Storkey[3]

[1]National Oceanography Centre, Empress Dock, Southampton SO14 3ZH, UK

[2]Mercator Ocean International, 2 Av. de l'aérodrome de Montaudran, Toulouse, France.

[3]Met Office, FitzRoy Road, Exeter EX1 3LX, UK

Key points

- The z~ time-filtered vertical coordinate is tested in a global 1/4-degree forced NEMO configuration.
- We confirm that z~ converts eulerian vertical velocities on time scales of a few days into coordinate displacements.
- z~ tends to reduce temperature and salinity biases, particularly at thermocline depths, without adverse effects on other metrics

Abstract

A recognized deficiency of ocean models with a constant-depth vertical coordinate is for truncation errors in the advection scheme to result in spurious numerical mixing of tracers, which can be substantial larger than that prescribed by the model's mixing scheme. The z~ vertical coordinate allows vertical levels to displace in a lagrangian fashion on time scales shorter than a few days, but reverts to fixed levels on longer timescales, and is intended to reduce numerical mixing from transient vertical motions such as internal waves and tides. An assessment of z~ in a ¼° global implementation of the NEMO model is presented. It is shown that, in the presence of near-inertial gravity waves in the North Atlantic, z~ significantly reduces eulerian vertical velocities with respect to those in a control simulation with the default z* vertical coordinate; that the vertical coordinate approaches an isopycnal, or adiabatic, surface on short timescales; and that both tendencies are enhanced when the z~ timescale parameters are lengthened with respect to the default settings. Evaluation of an effective diapycnal diffusivity, based on density transformation rates, shows that numerical mixing is consistently reduced as the z~ timescales are lengthened. The realism of the model simulation with different timescale parameters is assessed in the global domain, and it is shown that drifts in temperature and salinity, and the spindown in z*of the Antarctic Circumpolar Current, are reduced with z~, without incurring significant penalties in other metrics such as the strength of the overturning circulation or sea ice cover.

Plain Language Summary

In ocean models where the vertical coordinate is located at fixed depth levels, spurious, or non-physical, vertical numerical mixing of the temperature and

salinity fields is known to occur. A significant part of this is caused by "truncation errors" in the model code that cause spurious mixing when vertical motions in internal waves in the ocean repeatedly carry water parcels back and forth between the layers of the model. We investigate the z~ vertical coordinate, which flexes with internal waves on timescales shorter than a few days, but tends to fixed levels at long timescales, in an ensemble of integrations of a global NEMO model. We show that this consistently reduces biases in the temperature and salinity fields, particularly in the depth range 300-500m, and also reduces the unrealistic spin-down of the Antarctic Circumpolar Current, without significant adverse effects on other aspects of the model performance.

Keywords

Global ocean model; Numerical mixing; Vertical coordinates; Reduction of biases

1. Introduction

We may define numerical mixing in ocean models as mixing that does not arise from the explicit mixing scheme of the model. This extra spurious mixing may be as large as, or even substantially larger than, the explicit mixing in a given model (e.g., Megann, 2018), and has the potential to bias the representation of heat uptake by the ocean from the atmosphere in coupled climate models, as well as causing unrealistic drifts in internal temperature and salinity fields. Most of the numerical mixing is caused by truncation errors in the tracer advection scheme (Griffies et al, 2000), and manifests in several distinct ways, their relative severity depending on the model grid and the choice of numerical scheme. One manifestation is in the representation of deep overflows, such as those over the sills between the North Atlantic and the Arctic Ocean, and this is typically poor in models with a constant-depth vertical coordinate (Winton et al., 1998; Dickson et al., 2008; Ilıcak, 2016; Colombo et al., 2020). In this case, the spuriously high rate of entrainment of the overflow waters results in unrealistically warm and thick bottom waters downstream of the sills. This may be remedied by the use of terrain-following coordinates (e.g., Schchepetkin, 2005) or of isopycnic coordinates (Bleck and Smith, 1990; Megann et al., 2010). Another contribution is from numerical noise in the velocity field in regions where the mesoscale is poorly resolved, which tends to cause numerical instability in flow regimes with large cell Reynolds number (e.g., Bryan et al., 1975; Griffies and Hallberg, 2000; Ilıcak et al., 2012); this is a particular problem for global grids with "eddy-permitting" resolution of around ¼°, in which a large portion of the grid does not resolve the first Rossby radius (Hallberg, 2013). Megann and Storkey (2021, henceforth referred to as MS2021) demonstrated that increasing the biharmonic viscosity from the default value in a ¼° global NEMO model configuration consistently led to reductions in numerical mixing and in large-scale temperature drifts, without incurring penalties in most other metrics of model realism.

A third contribution to numerical mixing arises from net vertical advection of

tracers across coordinate surfaces by relatively high-frequency processes such as internal waves and tides. Near-inertial gravity waves (NIGWs, Alford et al., 2016) and internal tides (Wunsch, 1975) are typically characterized by periods of between 12 and 30 hours in nature, and their associated vertical velocities may reach several tens of meters per day. Such waves have the potential to contribute a significant fraction to the global ocean mixing budget when they break (Gargett and Holloway, 1984), but in general they propagate nearly adiabatically (i.e., without much mixing). In numerical models, by contrast, truncation errors in the vertical advection scheme tend to add an irreversible, or diffusive, component to tracer advection, and these transient vertical velocities add a spurious component to the vertical (or diapycnal) mixing (Leclair and Madec, 2011; Griffies et al., 2000). While this contribution to numerical mixing is an intrinsic property of fixed-coordinate models, pure isopycnic models, such as the Miami Isopycnic-Coordinate Model (MICOM, Bleck and Smith, 1990) and the Generalized Ocean Layered Dynamics model (GOLD; Hallberg and Adcroft, 2009), which use a potential density coordinate in the vertical, do not exhibit numerical mixing from this source, since vertical advection of tracers across coordinate surfaces is by construction zero in this model formalism. Such models, nevertheless, have disadvantages such as non-conservation of tracers due to the nonlinear equation of state, as well as poorly defined detrainment from the mixed layer.

In the last two decades, considerable effort has been put into developing models which combine the advantages of depth-coordinate and isopycnic models by using constant-depth levels in the upper ocean and isopycnic coordinates at depth; these include the Hybrid-Coordinate Ocean Model (HYCOM, Bleck, 2002) and version 6 of the Modular Ocean Model (MOM6, Adcroft et al, 2019). Controlled studies, in which a coupled model has a depth-coordinate ocean component replaced with an isopycnal model of the same resolution, have demonstrated that this type of model has reduced levels of numerical mixing from all three of the mechanisms mentioned above, when compared with comparable depth-coordinate models (Megann et al, 2010; Dunne et al, 2012), as evidenced by colder bottom temperatures, a sharper thermocline, and slower drifts in temperature and salinity fields, although Adcroft et al. (2019) report that issues still remain with the Denmark Strait overflow in MOM6 even when used with a hybrid vertical coordinate. Generalized Arbitrary Lagrangian-Eulerian frameworks (ALE: Adcroft and Hallberg, 2006, Griffies et al, 2020) provide a generalized approach to choosing the vertical coordinate most appropriate for each regime of the ocean: fixed-depth (either geopotential or terrain-following), where the divergence of lateral flow results in vertical velocities across the coordinate surfaces; quasi lagrangian, where the coordinate surface is displaced vertically according to the divergence of the flow; or some intermediate combination. This framework has the potential to approach an optimum configuration in terms of reducing numerical mixing from racer advection across coordinate surfaces, although in practice it may not be obvious what metrics might determine such an optimum.

The default vertical coordinate in version 4 of the Nucleus for European Mod-

elling of the Ocean model (NEMO v4, Madec et al, 2019) is the nonlinear free surface, or Variable Volume Layer (VVL), scheme (Stacey et al., 1995; Adcroft and Campin, 2004; Levier et al, 2007), usually referred to in shorthand as z*. This represents external gravity waves as changes to the layer vertical scale e_3 at each level scaled with the surface height anomaly over the water column. It allows the ocean volume to change as a result of mass fluxes through the surface, and so conserves tracers exactly, in contrast to the older linear free surface, provided some modifications to the leap-frog time stepping are implemented (Leclair and Madec, 2009). This coordinate system can be summarized as follows: barotropic vertical motion is quasi-lagrangian, in the sense that the external mode does not cause advection across the coordinate surfaces, while baroclinic vertical motion is quasi-eulerian, involving material advection across the coordinate interfaces, and it is the latter that contributes to numerical mixing. The z~ coordinate (Leclair & Madec, 2011, hereafter referred to as LM2011) is a modification to the z* vertical coordinate in NEMO in which the external mode, and internal motions at low frequencies, are treated within a eulerian framework as in z*, while internal vertical motions at high frequencies are represented as lagrangian. To clarify, at low frequencies internal vertical motions manifest as eulerian vertical velocities crossing the coordinate surface, while at high frequencies the coordinate surface itself is displaced, consistent with the divergence of the horizontal flow. The frequency division is accomplished by a first-order exponential filter, with a timescale $_{\sim}$ of a few days, while the z~ coordinate itself is restored to z* with a second timescale $_{z}$ of a few weeks. LM2011 demonstrated the effectiveness of z~ in an idealized channel domain in suppressing by a factor of five the numerical mixing from forced internal waves, although until the present study it has not been comprehensively tested in NEMO in a global domain. We note in passing a strong correspondence between z~ and the "slack" process in HYCOM (Bleck, 2002), where high-frequency internal waves in the near-surface geopotential layers of the hybrid grid are treated in a similar lagrangian way to reduce numerical mixing.

Several approaches have been used to quantify the sensitivity of numerical mixing to the vertical coordinate in idealized domains. Ilıcak et al. (2012) and Ilıcak (2016) used the Reference Potential Energy (RPE) method to analyze numerical mixing in a suite of model configurations in idealized domains, including lock exchange and a periodic channel: in the three models with fixed vertical coordinates, most of the numerical mixing was attributed to truncation errors in the advection scheme, with a relatively small contribution from cabbeling. In the pure isopycnic model (GOLD), by contrast, the only source of numerical mixing was the latter process. Petersen et al (2015) used the Model for Prediction Across Scales-Ocean (MPAS-Ocean) model as a platform to evaluate the choice of vertical coordinate on numerical mixing in some idealized test cases, comparing the unstructured-grid MPAS with the orthogonal-grid POP and MOM ocean models in z*, z~ with a 5-day time scale $_{\sim}$, terrain-following and pure isopycnic coordinate configurations, as well as in a global domain at several resolutions between 15 and 120 km. They used a similar potential energy metric to that em-

ployed in the studies by Ilıcak et al to diagnose the total mixing, concluding that MPAS-Ocean exhibited substantially lower numerical mixing than did POP or MOM, attributing the improvement partly to reduced truncation errors arising from the hexagonal grid used by their model, and partly to the implementation of the flux-corrected tracer transport (FCT) scheme on the MPAS-Ocean grid. Gibson et al (2017) applied the RPE approach to lock exchange simulations based on the MPAS-Ocean, MITgcm, MOM5 and MOM6 models, and separated the contributions of horizontal and vertical tracer advection to spurious mixing. They found that increasing horizontal resolution reduced the numerical mixing from horizontal advection, but this was not strongly sensitive to the choice of advection scheme; instead, reducing grid-scale vertical velocity noise had a stronger effect, consistent with the results of Ilıcak et al. (2012) and of MS2021. The numerical mixing was found to be much more strongly sensitive to the choice of vertical coordinate: the z~ cases showed reductions in spurious mixing from both horizontal and vertical advection, that from the former being attributed to the coordinate surface on short timescales being more closely aligned with isopycnal surfaces.

Holmes et al. (2021) evaluated an internal heat budget in individual water columns during runtime in a suite of simulations using the MOM5 depth-coordinate ocean model and the CICE sea ice model at 1/4° and 1/10° horizontal resolution and several choices of vertical resolutions, as well as a range of parameter settings for vertical and isoneutral diffusion schemes. From the heat budget they derived an estimate of numerical mixing in temperature classes, and concluded that the numerical contribution to the diathermal heat transport was of comparable magnitude to that associated with explicit parameterizations. Numerical mixing was found to be particularly prominent in the tropical thermocline, where it was sensitive to the vertical diffusivity and resolution, and they ascribed this to a combination of large vertical and horizontal temperature gradients and noise in the velocity field at the grid scale, particularly in its horizontal components.

Lee et al. (2002), Urakawa and Hasumi (2014) and Megann (2018) used the density transformation framework of Walin (1982) to derive a zonal mean effective diapycnal diffusivity in domains with realistic boundaries and forcing, which was compared with the explicit diffusivity derived from the subgrid mixing scheme. This approach has the advantage, relative to the potential energy approaches mentioned above, of allowing analysis of a fully forced, and hence more realistic, model configuration, more similar to the situation in a climate model than in the spin-down and spin-up simulations of the former studies. Megann (2018) applied this technique to an eddy-permitting global NEMO configuration, finding that the rate of density transformation in the model was in some regions several times larger than that prescribed by the explicit mixing alone, and that the effective diffusivity was between 5 and 10 larger than the explicit diffusivity in density classes typical of intermediate and deep waters, and in the tropics and mid-latitudes. This study associated the numerical mixing with transient vertical velocities of up to two orders of magnitude larger than the mean large-

scale upwelling and downwelling velocities, characterizing these vertical motions as having a horizontal length scale close to the grid scale, but as being coherent over more than 1000m in the vertical.

In this paper we use an ensemble of global ¼° forced NEMO integrations to investigate the efficacy of the z~ vertical coordinate in a realistic ocean domain. We use local, one-dimensional metrics to compare the performance of z~ in a region of the North Atlantic where near-inertial gravity waves (NIGWs) have large amplitudes, and to quantify the sensitivity of z~ to its two timescale parameters. We then evaluate global metrics, including the effective diapycnal diffusivity $_{\text{eff}}$, global watermass drifts and biases, large-scale circulation indices and ice cover, to confirm that z~ robustly reduces numerical mixing, and that it thereby has an overall positive effect on the realism of the model. The model code base and configuration are closely related to those used by MS2021, and we shall explicitly compare the effects of z~ on large scale metrics with those of increasing the viscosity in a configuration with the z* coordinate, as described in the latter paper.

In Section 2 we describe the model and the experimental design, and Section 3 is an overview of the analysis used in the paper. In Section 4 we use NIGWs in the North Atlantic as a testbed to verify the functioning of the z~ coordinate in this configuration. In Section 5 we present analysis of the sensitivity of the global fields and large-scale circulation of the model to the vertical coordinate, and Section 6 is a summary and discussion.

2. Model description and experimental design

2.1 Model description

The GO8p0.1 model configuration is a prototype testbed used in the development of the new generation of UK global ocean configuration beyond the sixth Coupled Model Intercomparison Project (CMIP6), under the Joint Marine Modelling Programme (JMMP), a partnership between the Met Office, National Oceanography Centre, British Antarctic Survey and Centre for Polar Observation and Modelling. It is based on the GO6/GO7 ocean configurations (Storkey et al, 2018), the former being the ocean component of the GC3.1 coupled model (Williams et al, 2018) and the UK Earth System Model (UKESM1, Sellar et al, 2019), the latter two models forming the UK's contribution to CMIP6. It has, as far as is feasible, the same physics and parameterizations as GO6/GO7, with two major exceptions. The first is that the code base for the ocean component has been upgraded from version 3.6-stable to version 4.0.1 of the Nucleus for European marine Modelling (NEMO, Madec et al, 2016) ocean model. The second is that the sea ice model is changed from CICE to the new Sea Ice modelling Integrated Initiative model (SI^3), which is based on version of 3 of the Louvain-le-Neuve Ice Model (LIM3, Rousset et al., 2015), and is now an integral part of the NEMO v4 code.

The model is otherwise identical to that in GO6/GO7; the latter configuration is described in detail in Storkey et al (2018), but we summarize the main features

here. The grid is the eORCA025 extended global 1/4° resolution grid (Barnier et al, 2006), with a quasi-isotropic bipolar grid with poles at land points in Siberia and Canada, a southern extension to allow simulation of the Antarctic ice shelves, and a Mercator projection grid elsewhere. We emphasize that, apart from the change in sea ice model, the physics and parameter choices are almost identical between the control simulation described by MS2021 and the z* control in the present ensemble.

The default viscosity scheme is a bilaplacian viscosity which has a reference value A_{Lm} =-1.5 x10^{11} m^4s^{-1} at the equator, with values reduced polewards as the cube of the maximum grid cell dimension in order to avoid instability in the momentum diffusion equation (see Griffies and Hallberg, 2000). Although MS2001 demonstrated that this choice of viscosity is lower than optimal, resulting in cell Reynolds numbers larger than the critical value over a significant portion of the model domain and hence higher numerical mixing, we maintain the default viscosity value to preserve traceability to earlier configurations. The horizontal pressure gradient scheme follows a standard density Jacobian formulation (Shchepetkin and McWilliams, 2003), selected by enabling ln_hpg_sco in the namelist.

Tracer advection is performed by second-order Flux Corrected Transport (FCT) scheme, also known as total variation diminishing (TVD; Zalesak, 1979), for both horizontal and vertical advection of tracers. We note that this is essentially the same scheme as used in the "TVD" experiments described by LM2011. Lateral diffusion of tracers is along isoneutral surfaces, with a coefficient of 150 m^2s^{-1}; the default in NEMO v4 is the scheme of Redi (1982), as implemented by Cox (1987). No mesoscale eddy parameterization scheme is used. The vertical mixing scheme is a modified version of the Turbulent Kinetic Energy (TKE) scheme (Gaspar et al, 1990; Madec et al, 2016), with a background vertical eddy diffusivity of 1.2×10^{-5} m^2s^{-1}, which decreases linearly with latitude from 15°N and 15°S towards the Equator. The current GO8 configuration has the tidal mixing parameterization of Simmons et al (2004), which was applied in GO6, but since it is not present in the standard NEMO v4 release, is added to GO6 as a development branch (see Appendix A for details of the model sources).

The ocean is initialized at rest from a 1995-2004 average of the EN4 climatology (Good et al., 2013). The initial state of the sea ice is derived from a "bootstrap" initialisation option in SI^3 which assigns sea ice wherever the initial SST is at the freezing point, with concentration 0.90 and thickness set to 3.0 m in the northern hemisphere and 1.0 m in the southern hemisphere. Surface forcing is with CORE2 interannual fields (Large and Yeager, 2009), with the following forcing frequencies: 6-hourly wind speed, air temperature and humidity; daily longwave and shortwave radiation, with a diurnal cycle applied to the latter; and monthly mean precipitation. This forcing is identical to that used in the experiments described by Megann (2018), by Storkey et al (2018) and by Megann and Storkey (2021). The experiments are integrated from 1976 to 2005, with the last ten years used for much of the analysis.

2.2 The z~ vertical coordinate

The configuration used here applies a set of modifications to the model code relating to the z~ coordinate: selecting z~ with the standard releases of either version 3.6-stable or NEMO v4 leads to rapid and terminal instabilities in the model. Using a Lagrangian formulation for the internal layers *de facto* requires a lateral advection term for thicknesses, which, as formulated by LM2011, was actually implemented as a 2^{nd} order centred scheme. This has the advantage of being quite simple, and ensures a "clean", linear split between barotropic and baroclinic contributions. However, the dispersive nature of this scheme can lead to strong variations in the vertical coordinate, and the scheme does not guarantee that layer thicknesses remain strictly positive. A number of modifications have, therefore, been added to the original LM2011 scheme:

- The existing centered formulation has been replaced by a Flux Corrected Transport (FCT) scheme. This does improves the stability and suppresses the need to use an overly large value of thickness Laplacian diffusion.
- Additional constraints on the regularity of the vertical layers have been implemented. Laplacian vertical and lateral diffusion of thicknesses make use of conditional schemes based on predefined thickness gradient thresholds. This preserves the Lagrangian behavior of the coordinate as much as possible (Toy and Randall, 2009).
- Over partial bottom cells, internal thicknesses are more prone to vanish. which is prevented here by an enhanced restoration towards the reference (eulerian) coordinate.

The various "corrective" fluxes arising either from the FCT scheme or lateral thicknesses diffusion do not guarantee that the total height matches the free surface estimate (Hallberg and Adcroft, 2009). We have chosen here a reconciliation based on an "upstream" correction of barotropic fluxes as proposed by Higdon (2005).

In the NEMO namelist an option is provided which ramps z~ down to zero at the equator to increase numerical stability, but it was found in the present implementation that the model was stable with z~ applied over the whole global grid, so this latter choice was used in all experiments.

2.3 Experimental strategy

An ensemble of experiments was integrated to determine the effect of changing from z* to z~, and also the sensitivity to the time filtering applied for the latter coordinate, as follows:

1. z~ compared with z*;
2. z~ cutoff time $_{\sim}$ extended from the default of 5 days up to 40 days;
3. z~ restoration time $_{z}$ extended from the default of 30 days up to 60 days.

The experiments are listed in Table 1, along with their respective suite identifiers on the Met Office's Rose/Cylc system and on the Managed Archive Storage System (MASS). With a timestep of 15 minutes, the *zstar* experiment completed a year of integration in between 15 and 16 hours. z~ was found to be stable with the same timestep as used with z*, in contrast with the experience of Gibson et al (2017), where stability issues in their implementation of MPA-Ocean forced a timestep of half that in their z* configuration to be used. Nevertheless, z~ in NEMO was found to incur a performance penalty in this configuration of between 15% and 18% in runtime relative to z*, which comes mainly from solving additional 3-D advection with flux limiting and a diffusion terms for internal thicknesses, and to a lower extent from the computation of time filtered fluxes..

3. Analysis

3.1 Coordinate displacement in internal waves

The main objectives of the z~ scheme are: firstly, to minimize net spurious vertical advection of tracers on timescales that are short compared with the cutoff time T_{cutoff}; and secondly for the vertical coordinate to more closely follow an adiabatic surface on these timescales. We note in passing that in an isopycnic model such as MICOM (Bleck and Smith, 1990), both of these hold by construction, and furthermore hold on all timescales. LM2011 demonstrated the effectiveness of z~ by implementing the scheme in an idealized channel model, and energizing internal waves with a monochromatic 12-hour period. In the present study, by contrast, the complexity of the bathymetry, coastlines and ocean dynamics in a global model make such a simple approach challenging: internal waves are naturally present with angular frequencies on a spectrum from the Coriolis frequency to the buoyancy frequency, and we might not expect *a priori* to find waves with appropriate frequency and monochromaticity to use in comparably meaningful tests to those described in the above paper. However, Blaker et al (2012) have noted that, in a similar NEMO implementation with the same horizontal resolution, near-inertial gravity waves (NIGW) are created at northern and western boundaries and propagate in an equatorward and slightly eastward direction across subtropical gyres. These have periods a few percent shorter than the inertial period at any given latitude, which is close to 12 hours at 55°N, increasing to about 30 hours at 20°N. The waves have a vertical structure at this resolution that is typical of the first baroclinic mode, and in the western half of the North Atlantic between 25°N and 45°N they have maximum vertical velocities at depths between 1,000 and 3,000 meters of up to 50 meters per day.

We shall use the NIGWs discussed above as a testbed to examine the performance of the model with respect to both of these objectives, and also to investigate the sensitivity of any improvements to the two timescale parameters in the z~ scheme. More specifically, we focus on a location in the subtropical North Atlantic where the amplitude of the waves is typically high: we select a water column at i=930, j=798, located at 55°W, 28.5°N, and on the vertical level k=55, which has a nominal depth in z* of 2,101m (see location marked in

Figure 1). We shall refer to the vertical velocity defined at a given coordinate level, which in the model advects tracers across the coordinate surface, as the eulerian vertical velocity. First of all, we compare the eulerian vertical velocity with the rate of change of the coordinate depth at the same position: if z~ is working as designed, it should at least partially replace the eulerian vertical velocities associated with the NIGWs with coordinate displacements. Secondly, we compare the displacements of the coordinate surface with those of the potential density $_2$ =36.955 kg m^{-3} surface, selected to lie close to the nominal depth of the k=55 level in the same water column, and which should therefore be a good approximation to a neutral surface at this location. For metrics evaluated at a single time, we shall use the mean over the first hour of the analysis period, namely the start of January 1996; for time series, we show hourly means during the first month of this period.

3.2 Diffusivity estimate from watermass transformation rate

The analysis, based on that of Lee et al. (2002), is identical to that described in Megann (2018) and used again in MS2021. For clarity, we shall briefly define in this section the main quantities that we shall evaluate in Section 4.

A zonally-integrated watermass transformation streamfunction $G(\Theta,)$ is defined as

$$G(\Theta,\rho) = \Psi(\Theta,\rho) + \frac{\partial}{\partial t}V(\Theta,\rho) \quad (1)$$

where $\Psi(\Theta,)$ is the overturning streamfunction at latitude Θ and potential density , and $V(\Theta,)$ is the volume south of Θ and below the isopycnal surface . Considering only the ocean interior (defined as those regions in density space with potential density higher than the maximum surface density over an annual cycle), and assuming that the density transformation is entirely due to diffusive processes, we define a zonal mean effective diffusivity $_{eff}$ as

$$\kappa_{\mathrm{eff}}(\Theta,\rho) = \frac{\int_{\rho_{\mathrm{max}}}^{\rho} \frac{\partial G(\Theta,\rho)}{\partial y}\mathrm{d}}{\int_{x_{\mathrm{Wax}}}^{x_E} \frac{\partial \rho}{\partial x}\mathrm{dx}} \quad (2)$$

where x_W and x_E are the westward and eastward limits, respectively, of the basin at latitude Θ, and y is the northwards spatial dimension, both expressed in meters. The zonal integrals are caried out in density classes. We emphasize that this method makes no assumptions about equilibrium, since unsteadiness is accounted for in the second term on the right-hand side of Equation (1), but it does assume for the sake of simplicity that the longitude dependence of the integrands does not introduce unwanted effects, which reduces the robustness of comparisons between $_{eff}$ and the explicit diffusivity $_{exp}$. In reality, as discussed by Lee et al (2002) and by Megann (2018), there are additional contributions to the transformation rate from the nonlinearity of the equation of state, namely cabbeling and thermobaricity, but these tend to be spatially quite localized (mainly in the Southern Ocean and the subpolar North Atlantic: see Klocker and McDougall, 2010). The analysis we present here neglects these contributions,

which tend to create negative values of the effective diffusivity in the latter regions.

We evaluate $_{eff}$ in the same set of potential density $_2$ classes as used by Megann (2018) and by MS2021, from 5-day means from the final ten years of the integrations (1996 to 2005), and compare this with the same quantity in the z* experiment. In the experiments with z~, the total effective meridional transport *vocetr_eff*, which is the sum of the 2nd order centred advective fluxes, an upstream corrective flux issued from the FCT scheme, and the "thickness diffusion" correction fluxes applied when the z~ coordinate is updated, was used for the calculation of the streamfunction in place of the simple advective flux.

3.3 Basin temperature and salinity biases

For z~ to be an acceptable vertical coordinate for forced and coupled ocean configurations in realistic domains it should, overall, not increase biases in the temperature and salinity fields relative to observations, nor should it create new watermasses that are not observed in the real ocean. If it reduces numerical mixing as intended, it should indeed tend to reduce the biases and drifts with respect to those found with z*. We will compare temperature and salinity censuses between the model experiments to confirm the first requirement, and present zonal mean temperature and salinity biases at selected depths with respect to climatological estimates to confirm the second condition. MS2021 demonstrated a strong correlation between the strength of the numerical mixing (quantified by the zonal and global means of the effective diffusivity $_{eff}$) in the closely related GO6 configuration, and the rate of cooling in the depth range 200-2,000 meters in the globally averaged temperature: reduced mixing (in this case effected by raising the viscosity) was associated with reductions in the rate of drift by up to 50%, even though the picture was complicated by large-scale warm biases in the upper 200 meters. This work also found that temperature and salinity biases of both signs at 300 m, a depth typical of the annual thermocline, were reduced (temperature more consistently than salinity) as the numerical mixing was reduced, and so we will directly compare the dependence of the biases at this depth on z~ and its time scale parameters with those resulting from increasing the viscosity.

4. Results

4.1 Vertical coordinate metrics

In the left-hand panels of Figure 1 we show the mean of the eulerian vertical velocity on level k=55, which has a nominal depth on the W grid of 2,023 meters, in the first hour of the analysis period; the center panels show the depth of this level on the W grid, and the right-hand panels show the rate of change of the depth of the level in m day^{-1}, evaluated from consecutive hourly means. The top row of panels shows results from z*, and the bottom panels results from the z~ experiment with default parameters, *ztilde_5_30*. The black circle on Figures 1(a) and (b) indicates the location of the water column at 27.5°N, 55°W

at which we shall quantitatively evaluate the time evolution of the wave fields in the following section. In the z* case (Figure 1(a)), the NIGWs are represented clearly as vertical velocities with amplitudes of more than 40m per day, and they have wavelengths of about 200km and periods between 18 and 20 hours. In the z~ case (Figure 1(d)), by contrast, the amplitude of the eulerian vertical velocity is reduced by at least a factor of 5. The depth of the level k=55 in the z* case (Figure 1(b)) is, as expected, not affected by the vertical velocity, but with z~ (Figure 1(e)) the imprint of the waves on the coordinate depth is clear, as are also that of the poorly-resolved grid-scale features close to the topography at the western boundary and along the mid-Atlantic Ridge, and that of internal waves close to the Equator (described in detail by Blaker et al., 2021).

To evaluate more qualitatively the effect of z~ on the model's response to large-amplitude internal waves, we focus on the water column at the location marked in Figure 1(a). Figure 2 shows hourly means of the vertical velocity at this point on the same depth level k=55, over the first month of 1996, overlain with the rate of change of the depth at this point, for z* and the five *z~ e*xperiments. The passage of trains of NIGWs with period of around 24 hours through this point is evident, with a modulation of the amplitude from very small values to more than 40 m/day over periods of between ten and fifteen days. The immediate impression given by Figure 2 is that, even with the default timescale parameters, the z~ coordinate transfers most of the eulerian motion in the z* case into coordinate displacements, and that this process becomes more nearly complete as the z~ timescales lengthen; in *ztilde_40_60*, the vertical velocity has been reduced almost to zero, while the time series of the rate of change of the coordinate depth is very similar to that of the vertical velocity in *zstar*. Table 2 lists the RMS value of these two quantities over the month, as well as the ratio of the RMS vertical velocity to that in *zstar*, and confirms these impressions, with a monotonic decrease in w_{rms} with lengthening timescales, the latter reaching in *ztilde_40_60*a fraction of only 4% of that in *zstar*. Since the filter timescale and the restoration timescale to z* both act as first-order filters on the coordinate depths, we would expect that, as the respective timescales are increased, more of the wave spectrum is represented as an adiabatic quasi-isopycnal process in the model, instead of as a eulerian velocity.

In Figure 3 we show time series of the depth anomaly of the k=55 level at the same location (black solid lines); the depth anomaly of the $_2$=36.955 isopycnal (dashed black lines), which lies close to this depth at this location; and the difference between these time series (red lines), for hourly means over the same period as that shown in Figure 2. In the *zstar* case, the coordinate surface remains stationary, and the isopycnal surface ripples up and down at the inertial period as the trains of NIGWs pass through this water column, superposed on longer-timescale displacements from eddies and planetary waves. As the z~ time scale parameters are lengthened, the isopycnal surface is displaced progressively less by the NIGWs: in ztilde_5_30, the maximum amplitudes of the ripples in the difference (red line) are of order 1-2 m, while in ztilde_40_60, they are between 0.3 and 0.5m.

For accuracy and stability of the z~ coordinate, we prefer the displacements of the coordinate surfaces to be small in a given timestep compared with the cell thickness. Figure 4 presents cumulative distributions of the ratio of the cell thickness in a single hourly mean of each cell to the thickness of the same cell in the experiments, over selected depth ranges. As might be expected, the widths of the distributions about a ratio of unity reduce with depth: the level thicknesses increase with depth (from 1 meter at the surface, 100m at 1,000m depth, to 200m at 5000m), while the displacements from internal waves will generally not increase in the same way. Figure 4 also confirms that in all depth ranges the displacements increase with the filter timescales in z~.

Turning to stability concerns, the tails of these distributions are of interest: Table 3 lists the fraction of the ratio of the coordinate displacements in the model experiments in the first hour of 1996 to the thickness of the respective cell in *zstar*, in the same period, in the depth range 0-30m. We note first of all that there are no cells with a thickness less than a fraction 0.2 of the z* thickness, so we conclude that vanishing cells are unlikely to occur with z~ in this global domain. Secondly, almost all of the large ratios (>0.8) occur in water deeper than 3000m, rather than on the shelves, and even in the handful (fewer than ten) cases where a large ratio occurs in water shallower than 100m it tends to be located towards the middle of the water column. Finally, ratios higher than 2.0 occur in a maximum of 8844 grid cells (a fraction $6\text{x}10^{-5}$ of the whole domain) in *ztilde_40-60*, and fewer in all the other experiments. Problems with stability were not found with any of the z~ integrations, so the fact that no vanishing cell thicknesses were seen implies that the rare occurrences of ratios higher than 2.0 is not likely to correspond to unphysical behavior.

4.2 Mixing analysis

If z~ performs as intended, and reduces the contribution of internal wave motions to numerical mixing, this should be quantifiable as a reduction in the rate of diffusive watermass transformation, evaluated as the effective diffusivity $_{eff}$ as described in Section 3 and defined in Equation 2. Figure 5(a) shows the ratios of the global mean effective diffusivity $_{eff}$ in potential density classes in each experiment to the explicit diffusivity $_{exp}$ in the respective experiment, while Figure 5(b) shows the ratios of the global mean effective diffusivity $_{eff}$ in potential density classes in each experiment to the same quantity in the z* control *zstar*. For the sake of clarity, results are not plotted for values of $_2$ lighter than 33.00 or denser than 37.05 kgm^{-3}. Figure 5(a) shows that the ratio of $_{eff}$ to $_{exp}$ is generally between around unity and a maximum at a density around $_2$=36.50 kgm^{-3}, a value typically intermediate between those of southward-flowing deep waters and of the northward-forcing intermediate waters. At this density the maximum ratio in *zstar* is about 6.8, while this falls to between 6.0 and 6.2 in the z~ experiments, a reduction of between 9% and 12%.

The ratios of the effective diffusivity $_{eff}$ in each experiment to $_{eff}$ in *zstar* (Figure 5(b)) show that there is a consistent tendency for z~ to reduce $_{eff}$ with

respect to that in the z* configuration over the density range between $_2 = 36.50$ and 36.9 kgm^{-3}, and that increasing the z~ timescales generally leads to lower values of $_{\text{eff}}$ over this density range. To quantify this sensitivity, in Figure 5(c) we plot the mean of the ratio of $_{eff}$ to $_{eff}$ in *zstar* over the density range from 36.50 to 36.9 kgm^{-3} (values are listed in Table 4) against the geometric mean of the two timescales, assigning a timescale of zero for z*. A reduction of just over 5% is obtained with both *ztilde_5_30* and *ztilde_10_30*, and the ratio continues to decrease as the timescales are lengthened, but little improvement is seen between *ztilde_20_60* and *ztilde_40_60*, suggesting that any further lengthening of the timescale parameters is not worthwhile.

Comparison between 5(b) and the corresponding Figure 7(c) in MS2021 reveals that the reductions in $_{eff}$ obtained by implementing z~ are of the same order as these resulting from increasing the biharmonic viscosity: doubling the fixed viscosity with respect to the default value or using the largest value of the Smagorinsky parameter C_{MSmag}=4 both gave reductions of about 10%, although tripling the fixed viscosity reduced the effective diffusivity further than any of the z~ settings.

4.3 Model drifts and biases

We have shown in the previous section of this paper that the z~ coordinate reduces numerical mixing, as diagnosed by the zonal mean effective diffusivity based on large-scale density transformations, and to an extent that is comparable to that found with increased diffusivities by MS2021. We would, therefore, expect z~ to have a qualitatively similar effect in reducing drifts and biases in the interior temperature, and possibly to a lesser extent in the salinity, to those seen in simulations with higher viscosities. In this section we shall compare the sensitivity of changes in tracer fields to z~ and its timescale parameters.

We firstly examine the sensitivity of property changes of the major water masses to the z~ parameters. If turning on the z~ coordinate results in changes to the large-scale temperature or salinity fields, we would require that the changes resulting from z~ act to oppose those seen in the drift in the control. Panels (a)-(c) of Figure 6 show global watermass volume censuses in m^3 in year 30 of *zstar*; *ztilde_5_30* and *ztilde_40_60*: the temperature and salinity discretization employed has fixed intervals of 0.05 K and 0.02 psu, respectively. The red ellipses in each panel of this figure indicate the approximate regions of the major watermasses in temperature-salinity space, based on the analyses of Worthington (1981) and of Emery and Meincke (1986). These water masses are, in order of decreasing typical temperatures, Western North Pacific Central Water (WNPCW); North Atlantic Central Water (NACW); South Pacific Central Water (SPCW); South Atlantic Central Water (SACW); Pacific Equatorial Water (PEW); Mediterranean Water (MW); South Atlantic Intermediate Water (SAIW); Antarctic Intermediate Water (AAIW); North Atlantic Deep Water (NADW); Circumpolar Deep Water (CDW); and Antarctic Bottom Water (AABW). The black contours are of potential density $_2$. The overall census

is qualitatively similar after thirty years in each of the experiments, and the maxima in population in the T/S classes after 30 years still correspond acceptably to those observed. Panels 6(d-f) show, respectively, the volume changes in the same T/S classes between years 1 and 30 of *zstar*; the volume differences between years 30 of *zstar* and *ztilde_5_30*; and the volume differences between years 30 of *zstar* and *ztilde_40_60:* reduced volume in any T-S cell is represented by red shading, and increased volume by blue shading. Although it is not obvious with this color scale, the changes in the mode waters in the z~ runs are of opposite sign to those of the drift in *zstar*: for example, AAIW has a tendency to cool in *zstar* (red shading at lower temperatures and blue shading at higher), while this tendency is reversed between *zstar* and *ztilde_5_30* and *ztilde_40_60*, with larger differences in *ztilde_40_60*. Larger drifts can be seen to occur in the intermediate, deep and bottom watermasses, the latter representing considerably higher volumes than the mode waters: although some artifacts from the vertical discretization can be seen as patches of rapidly alternating sign, particularly in the near-vertical "beam" of AAIW in the center left of panel (g), some systematic features are visible. For clarity, panels (g)-(i) show the same changes as in panels (d)-(f), but with the region in temperature and salinity space enlarged to focus on the densest watermasses. The clearest example is in NADW: in *zstar* (panel (g)), there is a drift to increased salinity, presumably through mixing with overlying waters, but this drift is opposed to a small extent in *ztilde_5_30* (panel (h)) and to a larger extent in *ztilde_40_60* (panel (i)). Similarly, the tendency to warming of central AABW in *zstar* is partially opposed in *ztilde_5_30* and in *ztilde_40_60*, with the latter having a substantially stronger effect. We conclude that z~ does not cause any significant unphysical modifications in interior watermass characteristics; and what changes it does induce are firstly opposite in sign to the drifts in the z~ integration, and secondly strnegthen with longer z~ timescales.

In Figures 7 and 8 we show the biases in the zonal mean temperature and salinity, respectively, over the period 1996-2005, interpolated vertically onto selected depth levels, with respect to the corresponding fields in the EN4 climatology, averaged over the same period and interpolated onto the same depth levels. We first discuss the biases in the *zstar* control. At the surface, there are large-scale warm biases in tropical and subpolar latitudes, with cold biases in latitude bands centered at 40°S and 30°N. As the depth increases, the magnitude of the temperature biases increases, and the warm bias at in the tropics and subtropics is replaced by a cold bias that grows to a maximum at around 500m then decreases with depth. There is a warm bias in the Southern Ocean at all depths that appears to be persistent in NEMO simulations at this resolution (Storkey et al., 2018; Williams et al., 2018). The large excursions north of 35°N are chiefly related to biases in the paths of the North Atlantic Current and the separated Kuroshio: the former tends to lie too far south as far north as Grand Banks, while the latter lies 2-3° further north than the observed location. South of 35°N, the simulations tend to be slightly too salty at the surface, and fresher at 300m and 500m depth, with the bias then reducing with depth. North of 35°N,

they are generally saltier than the observed ocean, at all depths, and the bias again shows complex features related to the circulation.

The effect of z~ on the biases, shown by the differences of the curves in Figures 7 and 8 from the solid black lines, can be seen to be relatively small at most latitudes and depths, compared with the biases themselves. Nevertheless, in the latitude range between 35°S and 35°N, quite large changes can be seen in the temperature biases in the thermocline (300m and 500m) that robustly act to reduce the magnitude of the biases of both signs (Figure 7(b) and (c)), and the effect increases monotonically with the z~ timescales: at 300m in particular, the cold bias reduces from between 0.3-0.6 K to 0.1-0.4 K, with about half the effect at 500m. Similarly, north of 40°N and between 60°S and 35°S, z~ reduces the warm biases by up to 30%. z~ has a smaller influence on warm biases at 1000m and deeper (Figure 7(d)-(f)), but again it generally ameliorates them. A consistent improvement can again be seen in the salinity biases, with the largest effect again seen at 300m (Figure 8(b)); despite the improvements being at most of order 10%, the tendency is for all the z~ curves to lie closer to zero than those for *zstar*.

To quantify the effect of z~ on the model tracer fields, Tables 5 and 6 list the global RMS temperature and salinity biases at the same depth levels as those used in Figures 7 and 8, with the right-hand column showing the percentage difference in the RMS bias between *zstar* and *ztilde_40_60*. At every depth, applying z~ reduces the global RMS bias in both temperature and salinity, and lengthening the z~ timescale from the defaults leads to further reductions, with the proportional reduction in temperature bias typically about twice that in salinity.

The strongest sensitivity of the temperature biases to z~ is seen at 300m (Figure 7(b)), so to investigate the spatial distributions of the biases, we plot in Figure 9 the global temperature and salinity biases at this depth over the same period (1996-2005). As was the case with the experiments with increased viscosity described by MS2021 (Figures 10 and 11 of that paper), implementing z~ with the standard parameters (Figures 7(b) and (e)) leads to a modest alleviation of the large-scale cold and fresh biases in the tropical and subtropical Atlantic and Pacific, while at the same time reducing the warm and salty biases in the North and South Pacific. Extending the z~ timescales from ztilde_5_30 to ztilde_40_60 gives a further improvement in both temperature and salinity at this depth (Figure 9(c) and (d)). The exception to this is in the subpolar North Atlantic, where a persistent cold bias over the path of the North Atlantic Current (NAC) develops with z~ and worsens as the timescales are lengthened; this is associated with a southward and eastward displacement of the path of the NAC (not shown). The cold bias is likely to be a systematic error related to the 1/4° resolution: Marzocchi et al (2015) found that in a comparable forced NEMO configuration, there was a large cold bias of up to 5K over the same region at 1° resolution, a cold bias over a reduced area at 1/4° and almost no large-scale bias at 1/12°.

4.4 Global metrics

In this section we discuss the sensitivity to z~ of other metrics, including global mean quantities, large-scale circulation, the simulation of the Equatorial Pacific, and ice cover. Figure 10 shows time series of annual means of the volume-weighted global mean temperature and salinity, and of area-weighted surface fields, including surface temperature (SST), salinity (SSS) and surface heat and freshwater fluxes. We note first of all that the dependence of these metrics on the z~ parameters is robust, in the sense that where there is a significant sensitivity the ordering of values of the respective metric among the experiments is consistent for every year of the integration, and in addition that the ordering is invariably such that the difference from the *zstar* control increases monotonically with increasing timescale parameters. The mean temperature (Figure 10(a)) has the clearest sensitivity to the z~ parameters: *zstar* (black line) shows a consistent cooling from 1900 onwards by about 0.1 K, which is reduced markedly by z~, with the temperature drop from 1980 to 2005 reduced by 22% in *ztilde_5_20* and by 70% in *ztilde_40_60*, although the lack of representation of anthropogenic changes in longwave radiation in the CORE2 dataset makes it difficult to comment on the relative realism of the temperature trends. The surface temperature (Figure 10(b)) reduces slightly with z~ with further reductions with longer timescale parameters. The downward heat flux (Figure 10(c)) becomes less negative as the z~ timescales are lengthened: the mean heat flux into the ocean from 1980 to 2005 increases by 0.21 Wm^{-2} from *zstar* to *ztilde_5_30* and by 0.59 Wm^{-2} from *zstar* to *ztilde_40_60*. We note that the ocean surface heat flux used here, 'hfds', does not include latent heat from melting or freezing of sea ice, or from the geothermal heat flux, so the heat budget is not completely balanced in this case. We may conclude that z~ causes the model to lose less heat to the atmosphere; the only mechanism for this to happen, for a fixed surface forcing dataset, is for the sea surface temperature to be cooler, which appears to be the case, at least in the global mean; examination of the zonal mean SST in the ensemble (Figure 7(a)) confirms that the surface cooling occurs mainly in the latitude bands 40-50°S and 35-60°N.

The global mean salinity (Figure 10(d)) is not strongly dependent on z~, with a slight tendency to increase at longer z~ timescales, and the downward freshwater flux from precipitation and river runoff minus evaporation (Figure 10(f)) has no significant sensitivity to z~: the only mechanism for a drift in the global mean salinity is then through the freshwater flux associated with surface salinity restoration (not included in the mean surface freshwater flux shown in Figure 10(f)), and this is confirmed by the opposite signs of the surface and depth-weighted mean salinity. As shown in Figure 8(a), the surface salinity bias is slightly fresh at high latitudes, and salty in the tropics, consistent with a tendency to increased salinity stratification in the upper ocean, but we stress that this is only a weak effect. Finally, the SSH (Figure (10(g)), which does not include steric terms, is about 2cm higher in *ztilde_5_20* than in *zstar*, but does not increase further in any of the other experiments.

The question then arises of how reduced vertical mixing would give rise to the SST changes shown in Figures 7(a) and 10(b). Figure 7 shows that the z~ simulations are generally warmer than the *zstar* control between 300m and 1000m depth in the subtropics and tropics (40°S-40°N), but cooler at the surface in the subpolar latitude ranges 40-60°S and 40-60°N; this is consistent with reduced downwards mixing at thermocline depths if the temperature decreases with depth at lower latitudes, but increases at higher latitudes. This is certainly the case in the Southern Ocean: south of about 50°S Antarctic surface water is colder than the underlying intermediate waters, whereas over most of the ocean the opposite holds.

Figure 11 shows the time evolution of the annual mean major large-scale transports in the model ensemble, including the AMOC strength at 26°N and at 45°N; the ocean heat transport (OHT) at 26°N and 45°N; and the ACC volume transport through Drake Passage. Table 7 lists the means of the above quantities over the period from 1996 to 2005, and the right-hand column lists the fractional change in the respective metric between *zstar* and *ztilde_40_60*.

As described by Storkey et al (2018), the strength of the Atlantic meridional overturning circulation (AMOC) in the GO6 configuration was strongly dependent on horizontal resolution, being about 4 Sv higher at 1/12° than at 1/4°, and is unrealistically strong in both cases compared with observations (e.g. Smeed et al., 2018). The AMOC at 26°N in *zstar* (Figure 11(a)) follows a very similar trajectory to that of the 1/4° GO6 simulation, albeit about 3 Sv weaker, which may be a consequence of the different sea ice model in GO8p0.1. The overturning is significantly weaker with z~ than with z*, with a reduction of about 1 Sv between *zstar* and *ztilde_5_30* and a further reduction of 0.5 Sv as the timescales are lengthened, corresponding to a fractional weakening of 6% over the 10-year analysis period. The sensitivity of the AMOC at 26°N to z~ is substantially stronger than that to increased viscosity, as observed by MS2021: in that study, only the experiment with the largest Smagorinsky viscosity showed a significant reduction in AMOC or ocean heat transport with respect to the control experiment. The large amplitude of the NIGWs at tropical and subtropical latitudes, as shown in Figure 1, would imply that the numerical diapycnal mixing from these could be substantial, and therefore amenable to mitigation by z~, but a causal link between midlatitude mixing and the overturning circulation is not clear.

The ocean heat transport (OHT) might be expected to be more sensitive than the AMOC to a reduction in mixing, since one would expect any increase in temperature stratification to result in a strengthening in the heat transport from an overturning circulation of a given strength. Looking at Figure 7, we see that at 26°N there is indeed a warming in the generally northward-flowing waters between 300m and 1000m in the z~ experiments, relative to zstar, with very small temperature changes at the surface or below 1000m. Despite this, the OHT at 26°N (Figure 11(b)) reduces in *ztilde_40_60* by about 0.1 PW, or by about 10% of that in *zstar*. It is not clear by which mechanism z~ weakens

the AMOC, but at the same time the reason why the latter is unrealistically strong in 1/4° NEMO simulations is not fully understood. The OHT at 26°N in the *zstar* control is within the range of values calculated by Jackson et al (2019) from a set of ocean reanalyses, but smaller than the 1.3 PW estimated by McDonagh et al (2010), so at this stage it is difficult to conclude that z~ robustly makes the heat transport more or less realistic than in the control z* simulation. Further north at 45°N, the AMOC strength (Figure 11(c)) is by contrast almost completely unaffected by z~, but the OHT (Figure 11(d)) is again weakened by z~.

The transport through Drake Passage (Figure 11(e)) does robustly increase as the z~ timescales lengthen: after the second year, the transport is consistently between 5 and 10 Sv stronger in *ztilde_5_30* than in *zstar*, with that for the shorter timescales having intermediate values. This reduction of the rate of the unrealistic spindown of the Antarctic Circumpolar Current (ACC), relative to that seen in the standard 1/4° NEMO configuration, is similar to that reported as a result of increased viscosity by MS2021, who argued that suppression of gridscale noise in the velocity field would reduce the advection of momentum out of the ACC, but this is unlikely to be the mechanism acting here. We postulate that in the present ensemble z~ reduces the numerical mixing from vertical velocities associated with the vigorous eddy field in the Southern Ocean, which is evident in the *zstar* control as effective diffusivities $_{\text{eff}}$ of more than five times the explicit diffusivity in density classes with $_2$>36.5 kg m^{-3} south of 45°S (see Figure 6(a) of MS2021).

4.5 Other large-scale metrics

Holmes at al. (2021) found relatively high levels of numerical mixing in warm water classes within 10° of the Equator, particularly in the central and eastern Pacific, which they ascribed to a combination of large vertical and horizontal temperature gradients and noise in the velocity field at the grid scale, particularly in its horizontal components. MS2021 showed that, in the GO6 model configuration with default viscosity, some of the largest values of the cell Reynolds number were found between 10°S and 10°N, and that the effective diffusivity $_{\text{eff}}$ was also relatively large in this region. In the top row of Figure 12 we show the standard deviation of the vertical velocity on an equatorial section in the Pacific down to 3500m depth in (a) *zstar*; (b) *ztilde_5_30*; and (c) *ztilde_40_60*. Consistent with our results for subtropical NIGWs in Section 4.1 and Figure 1, in *ztilde_5_30* the vertical velocity variation with time is reduced by about 35% with respect to that in *zstar*, and that in *ztilde_40_60* is reduced by between 70 and 80%. Nevertheless, the maximum vertical velocities are seen at a much deeper level than the equatorial thermocline, as represented by the 18°C isotherm, which in the present simulations slopes up from about 180m at the west of the basin to about 70m at the east, so would not be expected to contribute significantly to numerical mixing at the thermocline, nor to affect the strength of the Equatorial Undercurrent (EUC). In Figures 12(d)-(f) we show the temperature on the Equator in the upper 300m in the same three experi-

ments, and in Figures 12(g)-(i) the zonal velocity over the same depth range, where the EUC is characterized by large eastward velocities close to the thermocline depth. There is a small expansion of the thermocline east of 120°W in the experiments with z~, resulting in a cooling of about 1°C close to the surface and a comparable warming between 150m and 300m, but nowhere below 500m is there a temperature change of more than 0.05°C between *zstar* and *ztilde_40_60*. We conclude that z~, although operating as intended to curtail the vertical velocities associated with high-frequency waves, has only a limited effect on mixing close to the Equator.

Reducing the level of mixing in regions covered by sea ice for at least part of the year might be expected to affect the seasonal ice cover: MS2021 found that increasing the viscosity led to a small alleviation of the unrealistically low ice cover in the Arctic, although even at the largest viscosities used in their study the summer ice extent was only increased by about 12% and still lay below the lower observational bound. Despite the change of sea ice model in the present configuration from CICE to SI^3, and despite the fact that only minimal tuning of the ice model parameters was carried out for this configuration, the seasonal cycles, and their biases with respect to the HadISST climatology, are very similar to those shown by MS2021. In contrast to the sensitivity of sea ice to viscosity found in the latter study, however, we find that z~ has almost no effect on sea ice cover, nor on the sea ice volume: the NH 1996-2005 mean area changes by only -0.1% from *zstar* to *ztilde_40_60*; the mean NH volume by 0.7%; the mean SH area by +0.6%; and the mean SH volume by +2%. This is consistent with the zonal mean surface temperature bias shown in Figure 7(a), where almost no spread between the experiments can be seen south of 60°S or north of 60°N.

5. Summary and discussion

We have presented an assessment of the time-filtered z~ vertical coordinate, using an ensemble of experiments based on a 1/4° global configuration of the NEMO v4 ocean model. The control experiment uses the default z* fixed vertical coordinate, and the remaining five experiments use z~ with different choices of the two timescale parameters in the z~ scheme, namely the filter timescale $_{\sim}$ and the timescale for restoration of the vertical coordinate depths to the fixed z* depths $_{z}$; these vary from the default values of 5 days and 30 days, up to 40 days and 60 days, respectively. Lengthening these time scales permits vertical motions with increasingly long periods to be represented as displacements of the vertical coordinate, rather than as advective vertical velocities with their potential to cause numerical mixing of tracers, and also, because of the low-order filter used in z~, allows a larger portion of the wavelike behavior at any given frequency to be represented by the model as lagrangian or adiabatic. The analysis is divided into three parts: firstly, we have assessed the sensitivity of the z~ vertical coordinate to its timescale parameters in a single water column in the subtropical North Atlantic in the presence of near-inertial gravity waves. Secondly, we have evaluated the effective diapycnal diffusivity, as defined by density transformation rates, to quantify the effect of z~ and its parameter

settings on numerical mixing. Finally, we have investigated the realism of the simulation using a set of larger-scale metrics, including the representation and preservation of specific watermasses; temperature and salinity drifts; large-scale circulation indices; the Equatorial Pacific; and hemispheric sea ice cover.

Near-inertial gravity waves (NIGWs) are generated by wind power near the western boundaries of the subtropical gyres, with period close to the inertial period, and propagate eastward and equatorward. They are characterized by wavelengths of around 200km and by vertical velocities of several tens of meters per day, and in 1/4° simulations they manifest chiefly as the first baroclinic mode. We have used a grid cell at around 2,000m depth and in a location in the subpolar North Atlantic at 55°W and 27.5°N, where the NIGWs have consistently high amplitude, to investigate the effectiveness of z~ in the present implementation in translating eulerian vertical velocities into coordinate displacements, as well as assessing the sensitivity of this to the two timescale parameters. We have thereby confirmed that z~ achieves two essential targets: firstly, it reduces the vertical eulerian velocities associated with the NIGWs by a factor that increases from 3.5 with the default timescales to 15 with the longest timescales; and secondly, at this location the vertical coordinate at 2,000m depth approaches increasingly closely the $_2$=36.955 isopycnal surface, which is close to being a neutral and adiabatic coordinate at this depth, as the timescale parameters are increased. In this sense, we have demonstrated that z~ behaves increasingly like an isopycnal coordinate as the time scales are lengthened.

We have employed the mixing analysis of Megann (2018), evaluating an effective diffusivity $_{\text{eff}}$ as a function of latitude and potential density $_2$ for each experiment as a metric of the overall diapycnal density transformation rate, which includes contributions from both explicit and spurious numerical mixing. We have compared the global mean of this with the explicit diffusivity $_{\text{exp}}$ used in the model's mixing scheme, and with $_{\text{eff}}$ in the z* control: with z*, the effective diffusivity $_{\text{eff}}$ in density classes typical of intermediate and deep waters is between 4 and 8 times the explicit diffusivity, confirming the conclusions of previous studies that substantial numerical mixing occurs in this class of simulation. Lengthening the timestep parameters leads to progressive reductions in $_{\text{eff}}$ by a maximum of around 10% in the two experiments with the longest timescales, confirming that z~ ameliorates this contribution to numerical mixing, as intended. This is quantitatively comparable with the effect of increasing viscosity in a very similar configuration, as shown by Megann and Storkey (2021), and experiments with a combination of z~ and tripled biharmonic viscosity (not presented here) show that the benefits of the two changes are additive.

If z~ is to be useful in a global ocean model, it should first of all not create unphysical new watermasses, and secondly tend overall to reduce biases in temperature and salinity, both on basin scales and more locally. Finally, it should not adversely affect the realism of large-scale circulation indices. We have shown here that all the major ocean water masses are preserved over the 30-year integration, and that where there are drifts, z~ tends to reduce these,

and increasingly so as the timescales are increased. We have demonstrated that zonal mean biases in salinity and temperature at selected depth levels are generally reduced by z~, and at 300 meters depth where the zonally averaged changes are strongest, they tend to consistently reduce the large-scale temperature and salinity biases, with again an increasing effect with longer timescale parameter values. The strength of the Atlantic overturning circulation at 26°N is reduced by up to 10% by z~, which was deemed to represent an increase in realism, given the unrealistically strong transport in the z* control, although the effect on the ocean heat transport (OHT) was more equivocal, with z~ leading to a reduction in an OHC in z* that was already marginally weaker than that observed. Finally, a small amelioration of the spindown of the volume transport through Drake Passage was seen in the z~ experiments, consistent with a reduction in numerical mixing

LM2011 noted that, while computation of the pressure gradient on level geopotential surfaces in z* configurations of NEMO was quite straightforward, the sloping coordinate surfaces in z~ presented more of a challenge to the numerical solution, although they did not include any estimation of the pressure gradient errors in their simulations. The more rigorous techniques developed for terrain-following models (e.g. Schepetkin and McWilliams, 2003) are becoming considered more appropriate for the NEMO model, particularly in the context of ongoing work on localized hybrid z*-terrain-following coordinate systems for the sill overflow regions in the North Atlantic; these are also likely to offer benefits in cases using z~, although evaluating the consequences of truncation errors in the pressure gradient calculation that are not based on residual spurious time-mean circulation will be more challenging.

In Section 4.1, we showed that the fraction of grid cells in our z~ experiments where the change in the grid thickness from the z~ scheme was larger than a few tens of percent of the thickness in z* was less than 10^{-4}, although this fraction increased with longer z~ timescales. Our analysis of the response of the vertical coordinate in the presence of near-inertial gravity waves (NIGWs) showed that these waves caused the largest change in thickness of up to 10 m at depths below 1000m, where the z* level thickness in the model grid is at least 100m, so the relative distortion in this regime, at least, is small. Nevertheless, Petersen et al (2015) sounded a note of caution, reporting that, in their lock exchange experiments using z-tilde in the MPAS-Ocean model, significant distortion to the grid cells occurred, resulting in excessive numerical mixing. This is unlikely to be the case in the global domain we have described on a 1/4° grid, but where higher resolutions may permit more energetic vertical coordinate displacements it would be prudent to check that undesirable grid distortions do not occur to any significant extent.

In summary, the z~ coordinate, as implemented in the NEMO v4 branch we have used, performs as intended, and leads in general to an improvement in model realism, in particular reducing model drifts and the rate of spin-down of the Antarctic Circumpolar Current. However, we have demonstrated that

the default settings of the z~ timescale parameters of 5 days for $_{\sim}$ and 30 days for $_{z}$ result in only relatively small improvements, whereas lengthening both of these to 40 days and 60 days, respectively, strengthens its operation with no adverse effects. The numerical mixing resulting from inertial waves is likely to be more sensitive to the choice of the shorter of the two timescales (in this case $_{\sim}$), even though small improvements are still visible (notably in Figures 2(d) and (e), and in Figure 5(c)) between the *ztilde_20_30* and *ztilde_20_60* experiments where only $_{z}$ is changed. The effect of z~ appears to start to saturate in the two experiments with the longest time scale parameters, so there is unlikely to be an advantage in lengthening them further. The only significant drawbacks from z~ in this configuration are the increase of between 15% and 20% in run time relative to the standard z* case, and an increase in the cold bias in the north-western Atlantic, as shown in Figure 8, although the latter is likely to be a consequence of a systemic error in the path of the North Atlantic Current at the present resolution (e.g., Hirschi et al., 2020), rather than a bias introduced directly by z~. We may therefore recommend it, albeit with specific minor reservations, as a tool to reduce numerical mixing in 1/4° global simulations. At higher resolutions, where the amplitudes of vertical velocities associated with internal waves, eddies and equatorial waves are likely to be substantially larger than at 1/4°, and also particularly in simulations with tidal forcing, its benefits in reducing numerical mixing are likely to be proportionally larger, and the degradation in run speed from z~ may well be regarded as a negligible disadvantage.

Acknowledgments

This work has been carried out as part of the project "Reducing numerical mixing resulting from applying tides explicitly in a global ocean model" (RENUMERATE) under the Copernicus Marine Environment Monitoring Service (CMEMS). CMEMS is implemented by Mercator Ocean International, in the framework of a delegation agreement with the European Union. It was also co-funded by the Natural Environment Research Council (NERC) under the Climate Linked Atlantic Sector Science (CLASS) marine research program (NE/R015953/1), which supports the Joint Marine Modelling Programme (JMMP), a partnership between the Met Office, National Oceanography Centre, British Antarctic Survey and the Centre for Polar Observation and Modelling. The authors would like to thank Pierre Mathiot, Adrian New and Bablu Sinha for helpful suggestions and advice. The model was integrated on the MONSooN system, a collaborative HPC facility supplied under JMMP, while the analysis was carried out on the JASMIN platform, funded by NERC and maintained by the Centre for Environmental Data Analysis (CEDA).

Data availability

The derived data used for the analyses and plots are available at https://doi.org/10.5281/zenodo.6076410

The monthly output from the model integrations is archived on the UK Met Office Managed Archive Storage System (MASS), and available for research

use through the Centre for Environmental Data Analysis JASMIN platform (http://www.jasmin.ac.uk).

References

Adcroft, A. and Campin, J.-M., 2004: Rescaled height coordinates for accurate representation of free-surface flows in ocean circulation models, *Ocean Modelling*, **7**, 269–284, https://doi.org/10.1016/j.ocemod.2003.09.003.

Adcroft, A., and Hallberg, R., 2006: On methods for solving the oceanic equations of motion in generalized vertical coordinates**.** *Ocean Modelling*, **11(1-2)**, DOI:10.1016/j.ocemod.2004.12.007.

Adcroft, A., Anderson, W.G., Balaji, V., Blanton, C., Bushuk, M., Dufour, C.O., Dunne, J., P., Griffies, S.M., Hallberg, R. Harrison, M.,J., Held, I.M., Jansen, M., John, J.,G, Krasting, J.P., Langenhorst, A.R., Legg, S., Liang, Z., McHugh, C., Radhakrishnan, A., Reichl, B.G., Rosati, A., Samuels, B.L., Shao, A., Stouffer, R.,J., Winton, M., Wittenberg, A.T., Xiang, B., Zadeh, N. and Zhang, R., 2019: The GFDL Global Ocean and Sea Ice Model OM4.0: Model Description and Simulation Features. *Journal of Advances in Modeling Earth Systems*, **11(10)**, DOI:10.1029/2019MS001726.

Alford, M. H., Mackinnon, J. A., Simmons, H. L., and Nash, J. D., 2016. Near-inertial internal gravity waves in the ocean. *Annu. Rev. Marine Sci.* 8, 95–123. doi: 10.1146/annurev-marine-010814-015746

Blaker, A.T., J.J-M. Hirschi, B. Sinha, B. de Cuevas, S. Alderson, A. Coward, and G. Madec, 2012. Large near-inertial oscillations of the Atlantic meridional overturning circulation. *Ocean Modelling*, **42**. 50-56. 10.1016/j.ocemod.2011.11.008

Blaker, A.T. Hirschi, J.J.-M.; Bell, M.J.; and Bokota, A., 2021. Wind-Driven oscillations in the meridional overturning circulation near the equator. Part I: Numerical models. *J. Phys. Oceanog.* **51** (3). 645-661. https://doi.org/10.1175/JPO-D-19-0296.1

Bleck, R., and L. T. Smith, 1990: A wind-driven isopycnic coordinate model of the North and Equatorial Atlantic Ocean. 1: Model development and supporting experiments. *J. Geophys. Res.*, **95**, 3273-3285.

Bleck, R., 2002: An oceanic general circulation model framed in hybrid isopycnic-cartesian coordinates, *Ocean Modelling*, B, 55-88.

Bryan, K., S. Manabe, and R. C. Pacanowski, 1975: A global ocean atmosphere climate model. Part II. The oceanic circulation. *J. Phys. Oceanogr.*, **5**, 30–46.

Colombo, P., Barnier, B., Penduff, T., Chanut, J., Deshayes, J., Molines, J.-M., Le Sommer, J., Verezemskaya, P., Gulev, S., and Treguier, A.-M., 2020: Representation of the Denmark Strait overflow in a z-coordinate eddying configuration of the NEMO (v3.6) ocean model: resolution and parameter impacts, *Geosci. Model Dev.*, **13**, 3347–3371, https://doi.org/10.5194/gmd-13-3347-2020.

Cox, M. D., 1987: Isopycnal diffusion in a z-coordinate ocean model. *Ocean Modelling*, **74,** 1–5.

Dickson B., Meincke J., Rhines P., 2008. Arctic–Subarctic Ocean Fluxes: Defining the Role of the Northern Seas in Climate. In: Dickson R.R., Meincke J., Rhines P. (eds) Arctic–Subarctic Ocean Fluxes. Springer, Dordrecht. https://doi.org/10.1007/978-1-4020-6774-7_1

Dunne, J. P., J. John, A. Adcroft, S. M. Griffies, R. W. Hallberg, E. Shevliakova, R. J. Stouffer, W. F. Cooke, K. A. Dunne, M. J. Harrison, J. P. Krasting, S. Malyshev, P. C. D. Milly, P. Phillipps, L. T. Sentman, B. L. Samuels, M. J. Spelman, M. Winton, A. T. Wittenberg, and N. Zadeh, 2012. GFDL's ESM2 global coupled climate-carbon Earth System Models Part I: Physical formulation and baseline simulation characteristics. *Journal of Climate,* **25**(19), DOI:10.1175/JCLI-D-11-00560.1.

Emery, W.J. and Meincke, J., 1986. Global water masses: summary and review. *Oceanologica Acta* **9**: 383–391.

Gargett, A.E., and Holloway, G., 1984. Dissipation and diffusion by internal wave breaking. *J. Mar. Res* **42**, pp. 15-27. https://doi.org/10.1357/002224084788506158

Gaspar, P., Grégoris, Y., and Lefevre, J.-M.: A simple eddy kinetic energy model for simulations of the oceanic vertical mixing: tests at Station Papa and long-term upper ocean study site, *J. Geophys. Res.,* **95**, 16179–16193, doi:10.1029/JC095iC09p16179, 1990.

Gibson, A. H., A.M. Hogg, A.E. Kiss, C.J. Shakespeare, and A. Adcroft, 2017. Attribution of horizontal and vertical contributions to spurious mixing in an Arbitrary Lagrangian-Eulerian ocean model, *Ocean Modelling*, **119**, 45–56, doi:10.1016/j.ocemod.1564 2017.09.008.

Good, S. A., M. J. Martin and N. A. Rayner, 2013. EN4: quality controlled ocean temperature and salinity profiles and monthly objective analyses with uncertainty estimates, *JGR: Oceans*, **118**, 6704-6716.

Griffies, S., 2004: *Fundamentals of ocean climate models.* Princeton University Press, 434pp.

Griffies, S.M., R.C. Pacanowski and R.W. Hallberg, 2000. Spurious diapycnal mixing associated with advection in a z-coordinate ocean model. *Monthly Weather Review* **128** (3), 538-564.

Griffies, S., M., and W. Hallberg, R., 2000. Biharmonic friction with a Smagorinsky-like viscosity for use in large-scale eddy-permitting ocean models, *Mon. Wea. Rev.*, ***128***(8), 2935-2946.

Griffies, S.M., Adcroft, A., and Hallberg, R., 2020: A Primer on the Vertical Lagrangian-Remap Method in Ocean Models Based on Finite Volume Generalized Vertical Coordinates**.** *Journal of Advances in Modeling Earth Systems*, **12(10)**, DOI:10.1029/2019MS001954.

Hallberg, R. and A. Adcroft, 2009: Reconciling estimates of the free surface height in

Lagrangian vertical coordinate ocean models with mode-split time stepping. *Ocean*

Modelling **29**, 15–26, doi:10.1016/j.ocemod.2009.02.008.

Hallberg, R., 2013**:** Using a Resolution Function to Regulate Parameterizations of Oceanic Mesoscale Eddy Effects**.** *Ocean Modelling*, **72**, DOI:10.1016/j.ocemod.2013.08.007.

Higdon, R. L., 2005: A Two-Level Time-Stepping Method for Layered Ocean Circulation Models: Further Development and Testing. *J. Comp. Phys.*, **206(2)**, 463-504.

Hirschi, J.J.-M.; Barnier, B.; Böning, C.; Biastoch, A.; Blaker, A.T.; Coward, A.; Danilov, S.; Drijfhout, S.; Getzlaff, K.; Griffies, S.M.; Hasumi, H.; Hewitt, H.; Iovino, D.; Kawasaki, T.; Kiss, A.E.; Koldunov, N.; Marzocchi, A.; Mecking, J.V.; Moat, B. ; Molines, J.-M.; Myers, P.G.; Penduff, T.; Roberts, M.; Treguier, A-M; Sein, D.V.; Sidorenko, D.; Small, J.; Spence, P.; Thompson, L.; Weijer, W.; Xu, X., 2020.The Atlantic meridional overturning circulation in high resolution models. *Journal of Geophysical Research: Oceans*, **125 (4),** https://doi.org/10.1029/2019JC015522

Holmes, R. M., Zika, J. D., Griffies, S. M., Hogg, A. M., Kiss, A. E., and England, M. H., 2021. The geography of numerical mixing in a suite of global ocean models. *Journal of Advances in Modeling Earth Systems*, 13**,** e2020MS002333. https://doi.org/10.1029/2020MS002333

Ilıcak, M., 2016. Quantifying spatial distribution of spurious mixing in ocean models. *Ocean Modelling* **108** (2016) 30–38. http://dx.doi.org/10.1016/j.ocemod.2016.11.002.

Ilıcak, M., A.J. Adcroft, S.M. Griffies and R.W. Hallberg, 2012. Spurious dianeutral mixing and the role of momentum closure. *Ocean Modelling* **45–46**, 37–58. doi:10.1016/j.ocemod.2011.10.003

Jackson, L. C., Dubois, C., Forget, G., Haines, K., Harrison, M., Iovino, D., et al., 2019. The mean state and variability of the North Atlantic circulation: A perspective from ocean reanalyses. *Journal of Geophysical Research: Oceans*, **124**, 9141–9170. https://doi.org/10.1029/2019JC015210

Large, W. and Yeager, S., 2009: The global climatology of an interannually varying air–sea flux data set, *Climate Dynam.,* **33**, 341–364, https://doi.org/10.1007/s00382-008-0441-3.

Leclair, M. and G. Madec, 2009: A conservative leapfrog time stepping method, *Ocean Modelling*, **30**, 2–3, 88-94, https://doi.org/10.1016/j.ocemod.2009.06.006

Leclair, M. and G. Madec, 2011. z∼-Coordinate, an Arbitrary Lagrangian–Eulerian coordinate separating high and low frequency motions. *Ocean Modelling* **37,** 139–152.

Lee, M.-M., Coward, A.C., Nurser, A.G., 2002. Spurious diapycnal mixing of deep waters in an eddy-permitting global ocean model. *J. Phys. Oceanog.* **32**, 1522–1535.

Levier, B., A.-M. Tréguier, G. Madec, and V. Garnier, 2007: Free surface and variable volume in the nemo code. Tech. rep., MERSEA IP report WP09-CNRS-STR-03-1A, 47pp.
Madec, G., R. Bourdallé–Badie, P.A. Bouttier, C. Bricaud, D. Bruciaferri, D. Calvert, J. Chanut, E, Clementi, A. Coward, D. Delrosso, C. Ethé, S. Flavoni, T. Graham, J Harle, D. Iovino, D. Lea, C. Lévy, T. Lovato, N. Martin, S. Masson, S. Mocavero, J. Paul, C. Rousset, D. Storkey, A. Storto and M. Vancoppenolle, 2017. The NEMO Ocean Engine, doi: 10.5281/zenodo.1472482. Revision 8626, last retrieved 13 February 2019

Marzocchi, A.; Hirschi, J.J.-M.; Holliday, N.P.; Cunningham, S.A.; Blaker, A.T.; Coward, A.C., 2015 The North Atlantic subpolar circulation in an eddy-resolving global ocean model. *Journal of Marine Systems*, **142**. 126-143. https://doi.org/10.1016/j.jmarsys.2014.10.007

McDonagh, E. L., McLeod, P., King, B. A., Bryden, H. L., & Valdes, S. T. (2010). Circulation, heat, and freshwater transport at 36N in the Atlantic. Journal of Physical Oceanography, 40(12), 2661–2678. https://doi.org/10.1175/2010JPO4176.1

Megann, A. P., A. L. New, A. T. Blaker, and B. Sinha, 2010. The sensitivity of a coupled climate model to its ocean component. *J. Climate,* **23**, 5126–5150. https://doi.org/10.1175/2010JCLI3394.1

Megann, A., 2018. Estimating the numerical diapycnal mixing in an eddy-permitting ocean model. *Ocean Modelling* **121**, 19-33. DOI: 10.1016/j.ocemod.2017.11.001

Megann, A. and D. Storkey, 2021. Exploring viscosity space in an eddy-permitting global ocean model: is viscosity a useful control for numerical mixing? *Journal of Advances in Modeling Earth Systems*, **13**, https://doi.org/10.1029/2020MS002263

Petersen, M.R., D.W. Jacobsen, T.D. Ringler, M.W. Hecht and M.E. Maltrud, 2015. Evaluation of the arbitrary Lagrangian–Eulerian vertical coordinate method in the MPAS-Ocean model. *Ocean Modelling* **86** 93–113

Philander, S. G. H., Hurlin , W. J. and Pacanowski, R. C., 1986. Properties of long equatorial waves in models of the seasonal cycle in the tropical Atlantic and Pacific Oceans. *J. Geophys. Res.* **91** (C12): 207-214. doi:10.1029/JC091iC12p14207.

Redi, M. H., 1982: Oceanic isopycnal mixing by coordinate rotation. *J. Phys. Oceanogr.,* 12, 1154–1158.

Roullet, G. and Madec, G., 2000. Salt conservation, free surface, and varying levels: A new formulation for ocean general circulation models. *JGR-Oceans* **105**, C1. p23927-23942. https://doi.org/10.1029/2000JC900089

Rousset, C., Vancoppenolle, M., Madec, G. Fichefet, T., Flavoni, S., Barthélemy, A., Benshila, R., Chanut, J., Levy, C, Masson, S., and Vivier, F, 2015. The Louvain-La-Neuve sea ice model LIM3.6: global and regional capabilities. *Geosci. Model Dev.,* **8**, 2991–3005, 2015. https://doi.org/10.5194/gmd-8-2991-2015

Sellar, A.A., C.G. Jones, J. Mulcahy, Y. Tang, A. Yool, A. Wiltshire, F. O'Connor, M. Stringer, R. Hill, J. Palmieri, S. Woodward, L. Mora, T. Kuhlbrodt, S. Rumbold, D.I. Kelley, R. Ellis, C.E. Johnson, J. Walton, N.L. Abraham, M.B. Andrews, T. Andrews, A.T. Archibald, S. Berthou, E. Burke, E. Blockley, K. Carslaw, M. Dalvi, J. Edwards, G.A. Folberth, N. Gedney, P.T. Griffiths, A.B. Harper, M.A. Hendry, A.J. Hewitt, B. Johnson, A. Jones, C.D. Jones, J. Keeble, S. Liddicoat, O. , Morgenstern, R.J. Parker, V. Predoi, E. Robertson, A. Siahaan, R. Smith, R. Swaminathan, M. Woodhouse, G. Zeng, Guang and M. Zerroukat (2019). UKESM1: Description and evaluation of the UK Earth System Model. *Journal of Advances in Modeling Earth Systems*. (doi:10.1029/2019MS001739).

Shchepetkin, A.F., McWilliams, J.C., 2003. A method for computing horizontal pressure-gradient force in an oceanic model with a nonaligned vertical coordinate. *Journal of Geophysical Research* **108**, 1–34.

Simmons, H. L., S. R. Jayne, L. C. St. Laurent, and A. J. Weaver, 2004: Tidally driven mixing in a numerical model of the ocean general circulation. Ocean Modelling **6**, 245-263.

Smeed, D. A., Josey, S. A., Beaulieu, C., Johns, W. E., Moat, B. I., Frajka-Williams, E., et al. (2018). The North Atlantic Ocean is in a state of reduced overturning. *Geophys. Res. Lett.,* **45**, 1527–1533. https://doi.org/10.1002/2017GL076350

Stacey, M.W., Pond, S. and Z. P. Nowak, 1995. A numerical model of the circulation in Knight Inlet, British Columbia, Canada. *J. Phys. Oceanogr.*, **25**, 1037–1062.

Storkey, D., A.T. Blaker, P. Mathiot, A. Megann, Y. Aksenov, E.W. Blockley, D. Calvert, T. Graham, H.T. Hewitt, P. Hyder, T. Kuhlbrodt, J.G.L. Rae, and B. Sinha, 2018. UK Global Ocean GO6 and GO7: a traceable hierarchy of model resolutions. *Geosci. Model Dev.*, **11**, 3187–3213. DOI: 10.5194/gmd-11-3187-2018.

Toy, M.D. and Randall, D. A., 2008: Design of a Nonhydrostatic Atmospheric Model Based on a Generalized Vertical Coordinate. *Monthly Weather Review*, **137**, 2305-2330.

Trenberth, K. E., & Fasullo, J. T. (2017). Atlantic meridional heat transports computed from balancing Earth's energy locally. *Geophysical Research Letters*, **44**, 1919– 1927. https://doi.org/10.1002/2016GL072475

Urakawa, S. and H. Hasumi, 2013. Effect of numerical diffusion on the wa-

ter mass transformation in eddy-resolving models. *Ocean Modelling* **74**, 22-35. https://doi.org/10.1016/j.ocemod.2013.11.003

Walin, G., 1982. On the relation between sea-surface heat flow and thermal circulation in the ocean. *Tellus* **34**, 187-195.

Williams, K. D., Copsey, D., Blockley, E. W., Bodas-Salcedo, A., Calvert, D., Comer, R., Davis, P., Graham, T., Hewitt, H. T., Hill, R., Hyder, P., Ineson, S., Johns, T. C., Keen, A. B., Lee, R. W., Megann, A., Milton, S. F., Rae, J. G. L., Roberts, M. J., Scaife, A. A., Schiemann, R., Storkey, D., Thorpe, L., Watterson, I. G., Walters, D. N., West, A., Wood, R. A., Woollings, T. and Xavier, P. K., 2018. The Met Office Global Coupled Model 3.0 and 3.1 (GC3.0 & GC3.1) configurations. *J. Adv. Model. Earth Syst.. Journal of Advances in Modeling Earth Systems*, **9**. https://doi. org/10.1002/2017MS001115

Winton, M., Hallberg, R., and Gnanadesikan, A., 1998: Simulation of density-driven frictional downslope flow in z-coordinate ocean models, *J. Phys. Oceanogr.*, **68**, 2163–2174.

Worthington L.V. 1981. The water masses of the world ocean: some results of a fine-scale census. In: Warren BA and Wunsch C (eds) Evolution of Physical Oceanogra- phy, Ch. 2, pp. 42–69. Cambridge, MA: MIT Press.

Wunsch, C., 1975. Internal tides in the ocean. *Rev. Geophys.* **13**, p167-182. https://doi.org/10.1029/RG013i001p00167

Zalesak, S. T.: Fully multidimensional flux corrected transport algorithms for fluids, *J. Comput. Phys.,* **31**, 335–362, 1979.

Appendix A: Code documentation

The ocean model code is available from the NEMO website (www.nemo-ocean.eu) under the CeCILL free software license (http://www.cecill.info/). On registering, individuals can access the Fortran code using the open-source subversion software (http://subversion.apache.org/). The base code used for the integrations presented in this paper is merged from the following branches:

http://forge.ipsl.jussieu.fr/nemo/svn/NEMO/branches/UKMO/NEMO_4.0.4_mirror@10037

http://forge.ipsl.jussieu.fr/nemo/svn/NEMO/branches/UKMO/dev_r9950_GO8_package@10038

http://forge.ipsl.jussieu.fr/nemo/svn/NEMO/branches/UKMO/dev_r9950_GO6_mixing@10039

http://forge.ipsl.jussieu.fr/nemo/svn/NEMO/branches/UKMO/dev_r9950_old_tidal_mixing@10040

http://forge.ipsl.jussieu.fr/nemo/svn/NEMO/branches/2018/dev_r10057_ENHANCE03_ZTILDE@10643

The following preprocessing keys were applied in building GO8p0: key_trabbl; key_si3; key_zdftke; key_zdfddm; key_mpp_mpi; key_mpp_rep; key_nosignedzero; key_iomput

Experiment	Suite id	Vertical coord	$_{\sim}$ (days)	$_{z}$ (days)

Experiment	Suite id	Vertical coord	$_{\sim}$ (days)	$_{z}$ (days)
zstar	u-ba208	z*	N/A	N/A
ztilde_5_30	u-bm255	z~	5	30
ztilde_10_30	u-bs738	z~	10	30
ztilde_20_30	u-bs739	z~	20	30
ztilde_20_60	u-bs473	z~	20	60
ztilde_40_60	u-bs633	z~	40	60

Table 1: Summary of model experiments. The two numbers in the experiment name refer respectively to the z~ cutoff time parameter, $_{\sim}$, and to the restoration time to z*, $_{z}$. The "suite id" is the identifier for the model on the Managed Archive Storage System (MASS).

Experiment	w_{RMS} (m day^{-1})	w_{RMS} fraction of w_{RMS} in z*	z/ t_{RMS} (m day^{-1})
zstar	17.05	1.00	0.025
ztilde_5_30	3.752	0.22	17.74
ztilde_10_30	2.288	0.13	17.74
ztilde_20_30	1.373	0.08	17.74
ztilde_20_60	1.125	0.065	17.74
ztilde_40_60	0.6874	0.040	17.74

Table 2 Root-mean-squared quantities evaluated at 55°W, 27.5°N and at a nominal 2,000 meters depth over a month of hourly means: the RMS vertical velocity; the ratio of the latter to that in the z* control experiment; and the RMS rate of vertical displacement of the coordinate surface.

	<0.30	<0.40	>1.70	>1.9	>2.0
Ztilde_5-30	0	$1x10^{-5}$	$2x10^{-5}$	$3x10^{-6}$	$5x10^{-7}$
Ztilde_10-30	0	$5x10^{-5}$	$9x10^{-5}$	$2x10^{-5}$	$4x10^{-6}$
Ztilde_20-30	0	$16x10^{-5}$	$21x10^{-5}$	$5x10^{-5}$	$1.5x10^{-5}$
Ztilde_20-60	$1x10^{-5}$	$38x10^{-5}$	$39x10^{-5}$	$8x10^{-5}$	$3x10^{-5}$
Ztilde_40-60	$2x10^{-5}$	$85x10^{-5}$	$73x10^{-5}$	$16x10^{-5}$	$6x10^{-5}$

Table 3. Fraction of the ratio of the coordinate displacements in the model experiments in the first hour of 1996 to the thickness of the respective cell in *zstar,* in the depth range 0-30m.

Experiment	Mean $_{eff}$	Mean ratio to z*
zstar	9.28×10^{-5}	-
ztilde_5_30	8.685×10^{-5}	0.9411
ztilde_10_30	8.831×10^{-5}	0.9496
ztilde_20_30	8.838×10^{-5}	0.9262
ztilde_20_60	8.584×10^{-5}	0.9165
ztilde_40_60	8.554×10^{-5}	0.9158

Table 4. The global mean effective diffusivity $_{eff}$ in each of the experiments (column 2), and the ratio of $_{eff}$ to that in *zstar* (column 3).

	zstar	*ztilde_5_30*	*ztilde_10_30*	*ztilde_20_30*	*ztilde_20_60*	*ztilde_40_60*	change
Surface	0.2387	0.2353	0.2813	0.2289	0.2276	0.2274	-4%
300m	0.5275	0.4760	0.4642	0.4471	0.4543	0.4461	-15%
500m	0.4805	0.4573	0.4458	0.4289	0.4286	0.4239	-12%
1,000m	0.3841	0.3629	0.3507	0.3473	0.3406	0.3431	-11%
2,000m	0.2332	0.2193	0.2133	0.2099	0.2089	0.2106	-10%
3,000m	0.1294	0.1225	0.1245	0.1213	0.1200	0.1204	-7%

Table 5: RMS temperature biases in K in 1996-2005 of model experiments at selected depth levels, with respect to the same period in the EN4 climatology, with the final column showing the percentage difference in RMS bias between *zstar* and *ztilde_40_60*.

	zstar	*ztilde_5_30*	*ztilde_10_30*	*ztilde_20_30*	*Ztilde_20_60*	*ztilde_40_60*	change
Surface	0.3755	0.3707	0.3688	0.3662	0.3673	0.3663	-2%
300m	0.1479	0.1413	0.1384	0.1373	0.1368	0.1373	-7%
500m	0.1209	0.1159	0.1146	0.1139	0.1136	0.1139	-6%
1,000m	0.0729	0.0700	0.0686	0.0674	0.0668	0.0667	-9%
2,000m	0.0493	0.0475	0.0471	0.0468	0.0467	0.0467	-5%
3,000m	0.0195	0.0189	0.0188	0.0186	0.0186	0.0185	-5%

Table 6: RMS salinity biases in psu in 1996-2005 of model experiments at selected depth levels with respect to the same period in the EN4 climatology, with the final column showing the percentage difference in RMS bias between *zstar* and *ztilde_40_60*.

	zstar	*ztilde_5_30*	*ztilde_10_30*	*ztilde_20_30*	*ztilde_20_60*	*ztilde_40_60*	cha
AMOC at 26°N	21.50	20.78	20.45	20.34	20.22	20.18	-6%
OHT at 26°N	0.9235	0.8875	0.8713	0.8586	0.8552	0.8431	-9%

	zstar	*ztilde_5_30*	*ztilde_10_30*	*ztilde_20_30*	*ztilde_20_60*	*ztilde_40_60*	cha
AMOC at 45°N	18.03	17.91	18.06	18.03	18.01	17.91	-0.(
OHT at 45°N	0.5657	0.5259	0.5157	0.5056	0.4987	0.4937	-13
ACC transport	125.3	127.5	128.6	130.6	130.7	131.1	+5

Table 7. Means of transports from 1996 to 2005 in the model ensemble: AMOC strength at 26°N in Sv; OHT at 26°N in PW; AMOC strength at 45°N in Sv; OHT at 45°N in PW; and ACC transport in Sv. The right-hand column lists the change in the respective metric between *zstar* and *ztilde_40_60*.

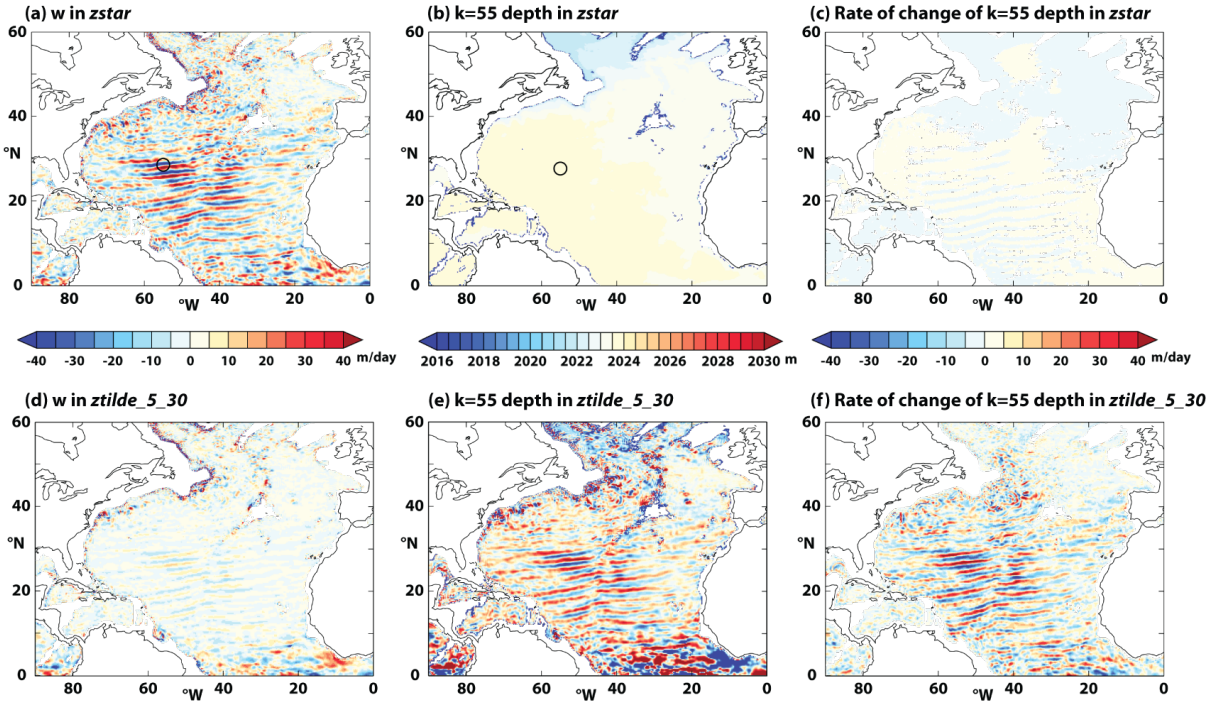

Figure 1. (a) The eulerian vertical velocity in m day $^{-1}$ at level k=55 with nominal depth closest to 2,000m in *zstar*; (b) the depth in m of level k=55 surface in *zstar*; (c) the rate of change of depth of this coordinate surface in m day $^{-1}$ in *zstar*; (d) The eulerian vertical velocity in m day $^{-1}$ at level k=55 in *ztilde_5_30*; (e) the depth in m of level k=55 surface in *ztilde_5_30*; and (f) the rate of change of depth in m day^{-1} of this coordinate surface in *ztilde_5_30*. The black open circles in panels (a) and (b) denote the location of the water column used for analysis.

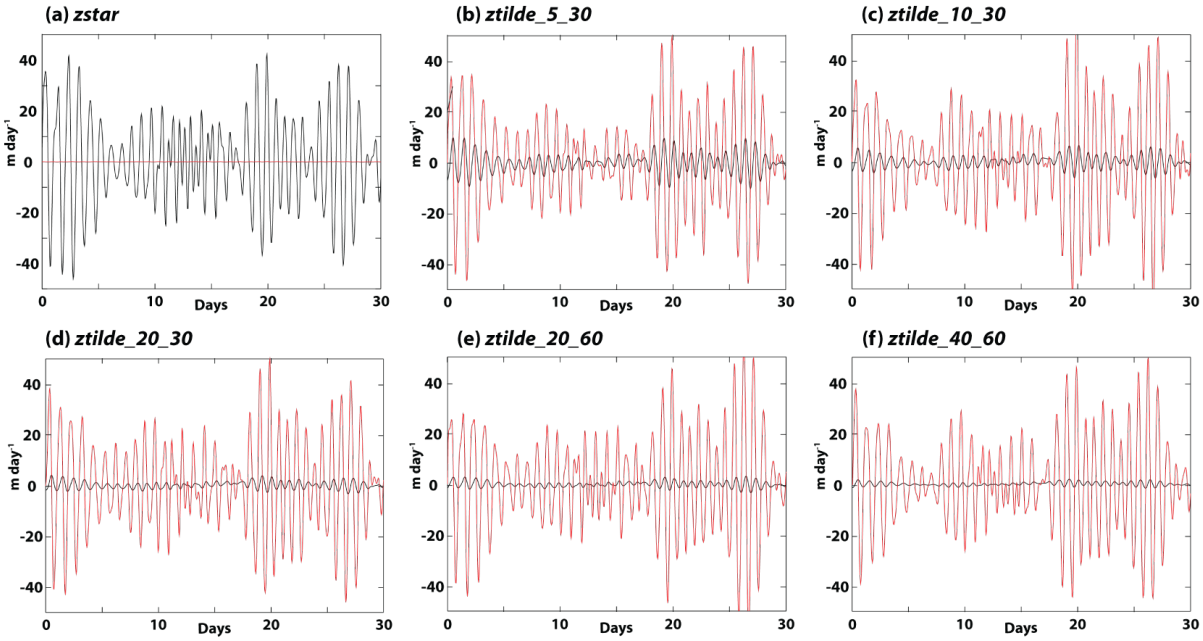

Figure 2. The eulerian vertical velocity in m day^{-1} on the depth level k=55 with nominal depth closest to 2,000m (black lines) and the rate of change of depth in m day^{-1} of the same surface in hourly means of (a) zstar; (b) *ztilde_5_30*; (c) *ztilde_10_30*; (d) *ztilde_20_30*; (e) *ztilde_20_60*; and (f) *ztilde_40_60*.

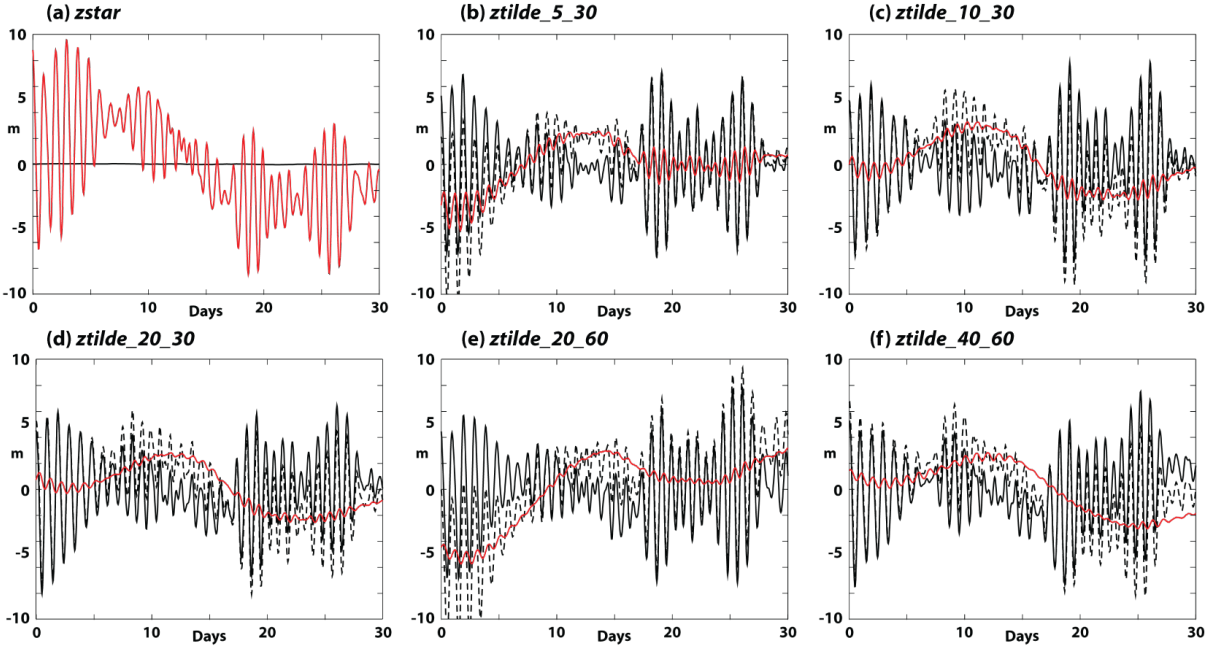

Figure 3. The hourly depth anomaly of the k=55 coordinate surface (solid black lines), the depth anomaly of the $_2$=36.955 isopycnal surface (dashed black lines), and the difference between the two (solid red lines) in (a) *zstar*; (b) *ztilde_5_30*; (c) *ztilde_10_30*; (d) *ztilde_20_30*; (e) *ztilde_20_60*; and (f) *ztilde_40_60*.

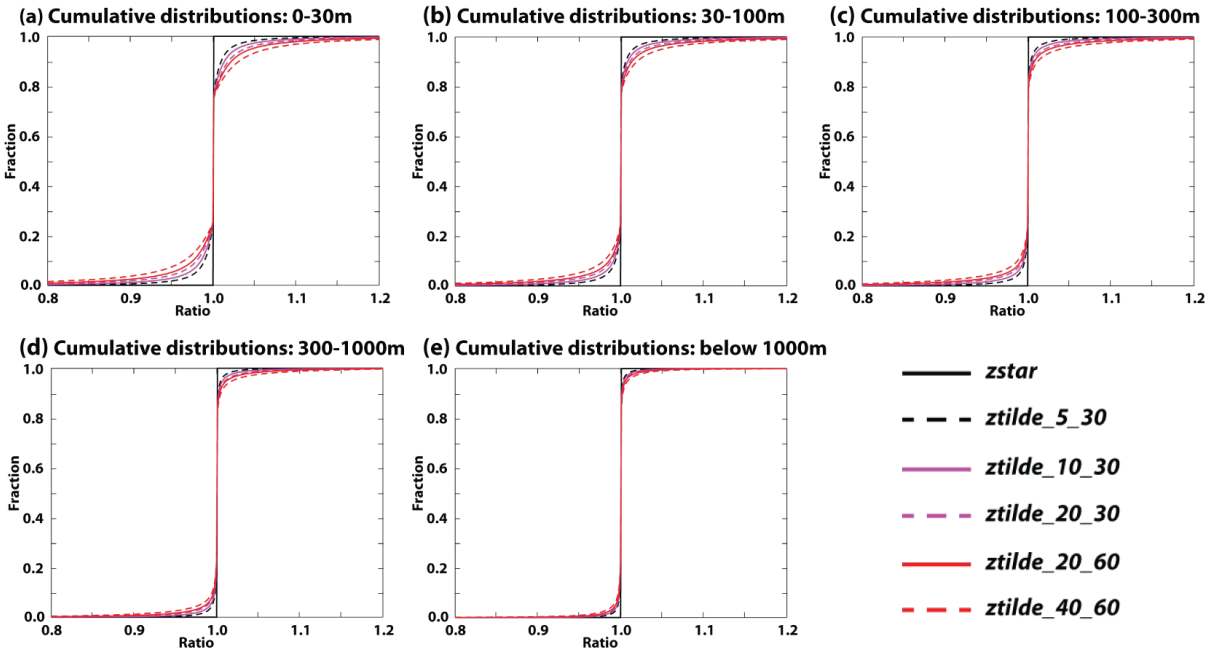

Figure 4. Cumulative histograms of the ratio of the cell thickness in the model experiments in the first hour of 1996 to the thickness of the respective cell in *zstar* in selected depth ranges: (a) 0-30 m; (b) 30-100 m; (c) 100-300m; (d) 300-1,000 m; and (e) below 1,000 m.

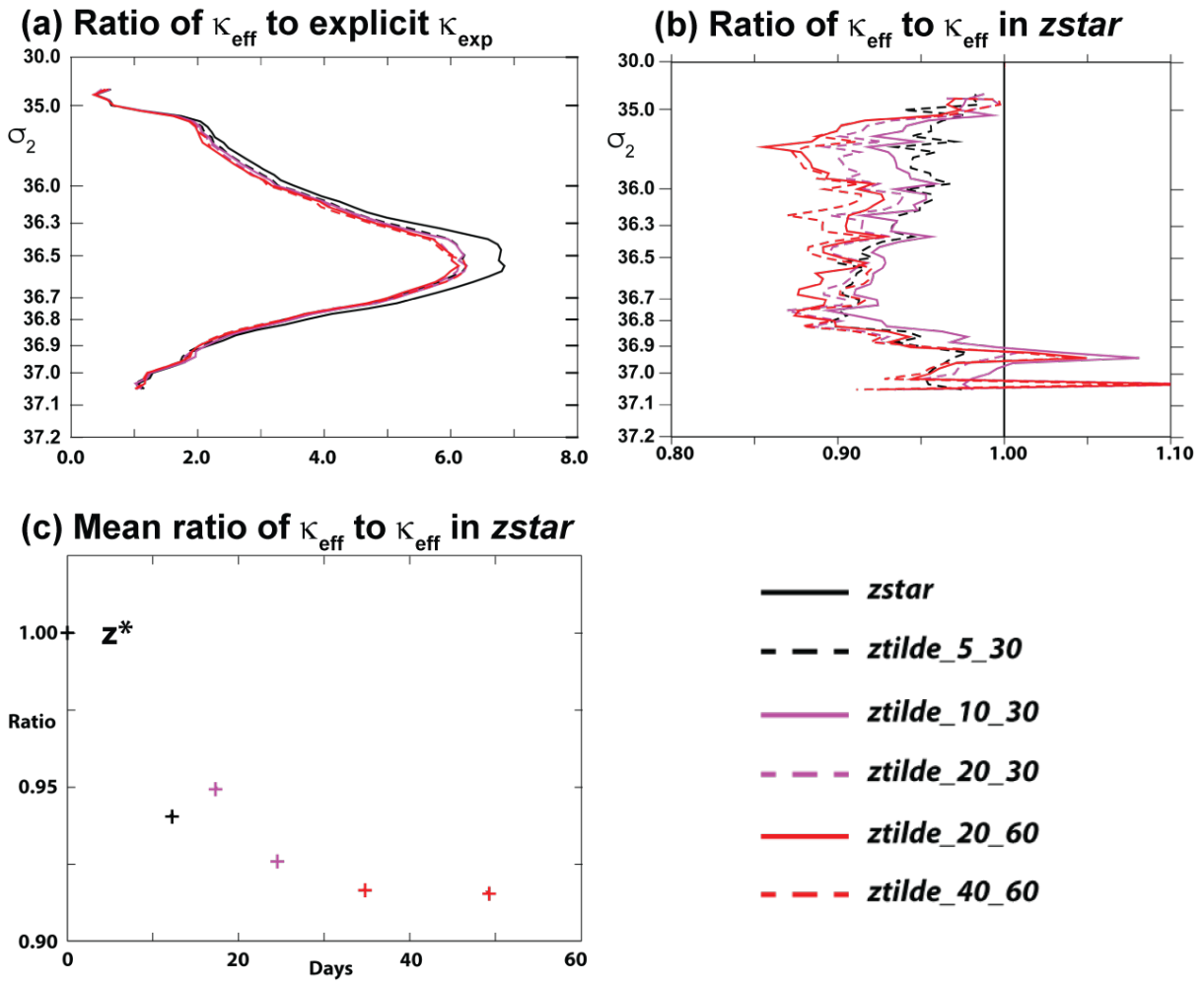

Figure 5. Ratios of global mean effective diffusivities $_{\text{eff}}$, evaluated in potential density classes: (a) ratios to the respective explicit diffusivity $_{\text{exp}}$; and (b) ratios to $_{\text{eff}}$ in *zstar*; (c) Scatter plot of the mean $_{\text{eff}}$ to $_{\text{eff}}$ in z* control in the density range $36.50 < {}_{2} < 36.9$ kgm^{-3} against the harmonic mean of the two z~ time scales (defining this to be zero for the *zstar* experiment).

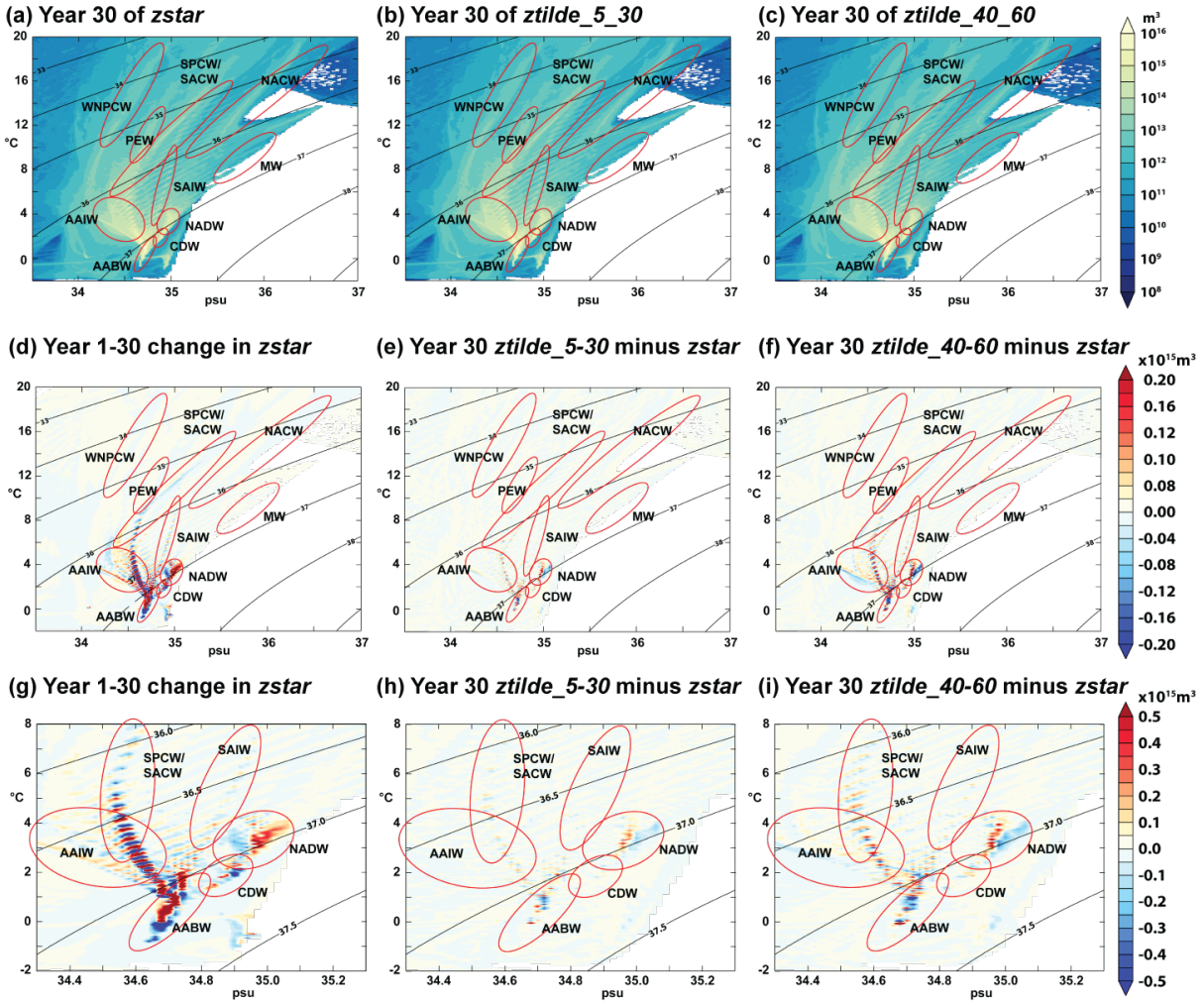

Figure 6. Watermass volume censuses: volumes in temperature and salinity classes in m^3 (on a logarithmic scale) in year 30 of (a) *zstar*; (b) *ztilde_5_30*; and (c) *ztilde_40_60*; (d) volume changes between year 1 and year 30 of *zstar*; (e) volume differences in year 30 of *ztilde_5_30* from those in the same year of *zstar*; and (f) volume differences in year 30 of *ztilde_40_60* from those in *zstar*. Panels (g)-(i) are identical to panels (d)-(f), but focus on the densest watermasses, and are shown on a narrower color scale. Red ellipses indicate approximate T/S ranges of selected watermasses (the acronyms are expanded in the text), and black lines are contours of potential density $_2$.

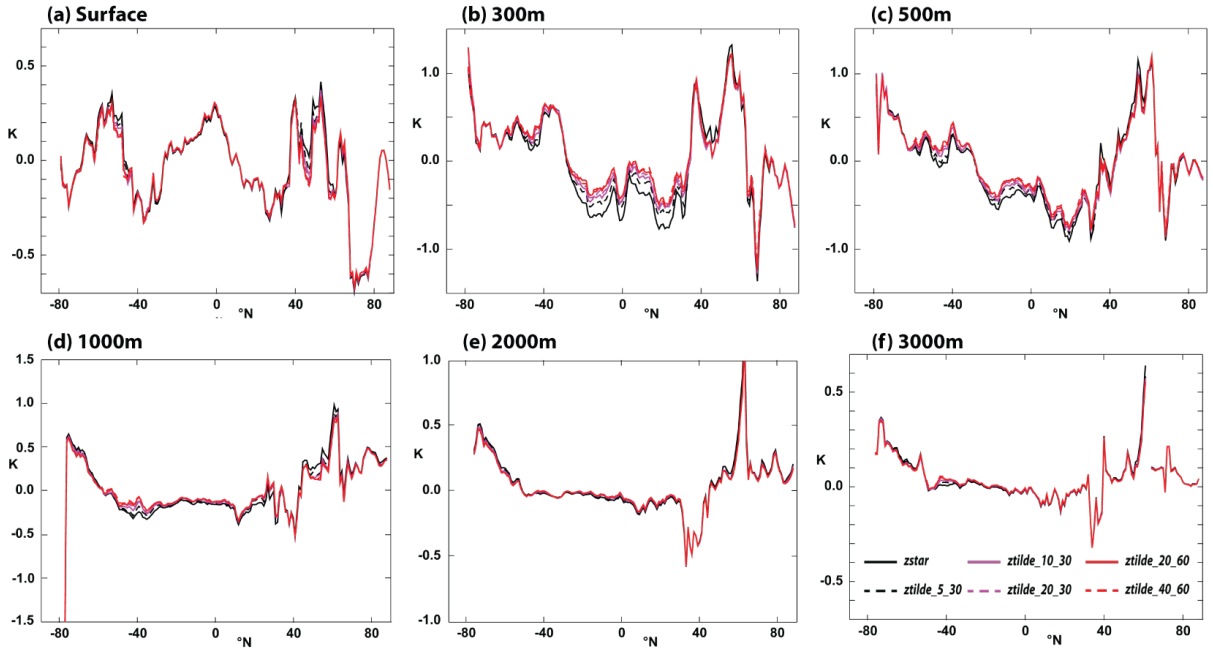

Figure 7. Zonal mean temperature biases in K of each of the experiments evaluated in 1996-2005 with respect to the EN4 climatology at (a) the surface level; (b) 300m; (d) 500m; (d) 1,000m; (e) 2,000m; and (f) 3,000m.

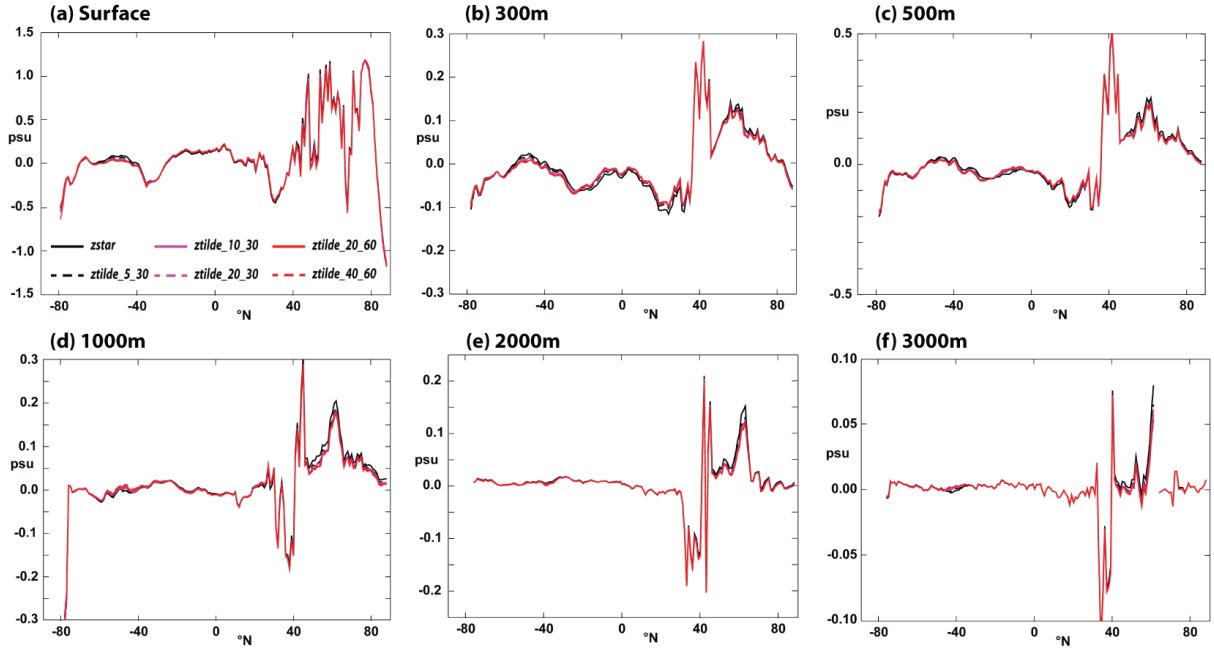

Figure 8. Zonal mean salinity biases in psu of each of the experiments evaluated in 1996-2005 with respect to the EN4 climatology at (a) the surface level; (b) 300m; (d) 500m; (d) 1,000m; (e) 2,000m; and (f) 3,000m.

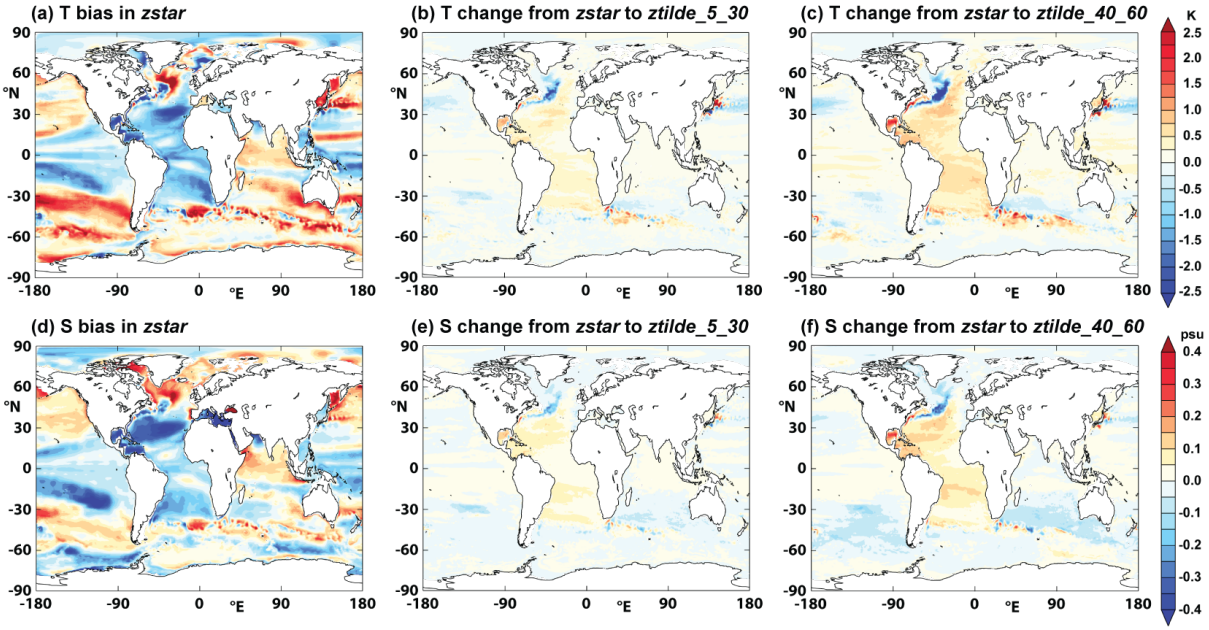

Figure 9. (a) Global temperature bias in K at 300m in 1996-2005 with respect to EN4 in *zstar*; temperature differences from *zstar* in (b) *ztilde_5_30*; and in (c) *ztilde_40_60*; (d) global salinity bias in psu at 300m with respect to EN4 in *zstar*; salinity differences from *zstar* in (e) *ztilde_5_30*; and in (f) *ztilde_40_60*.

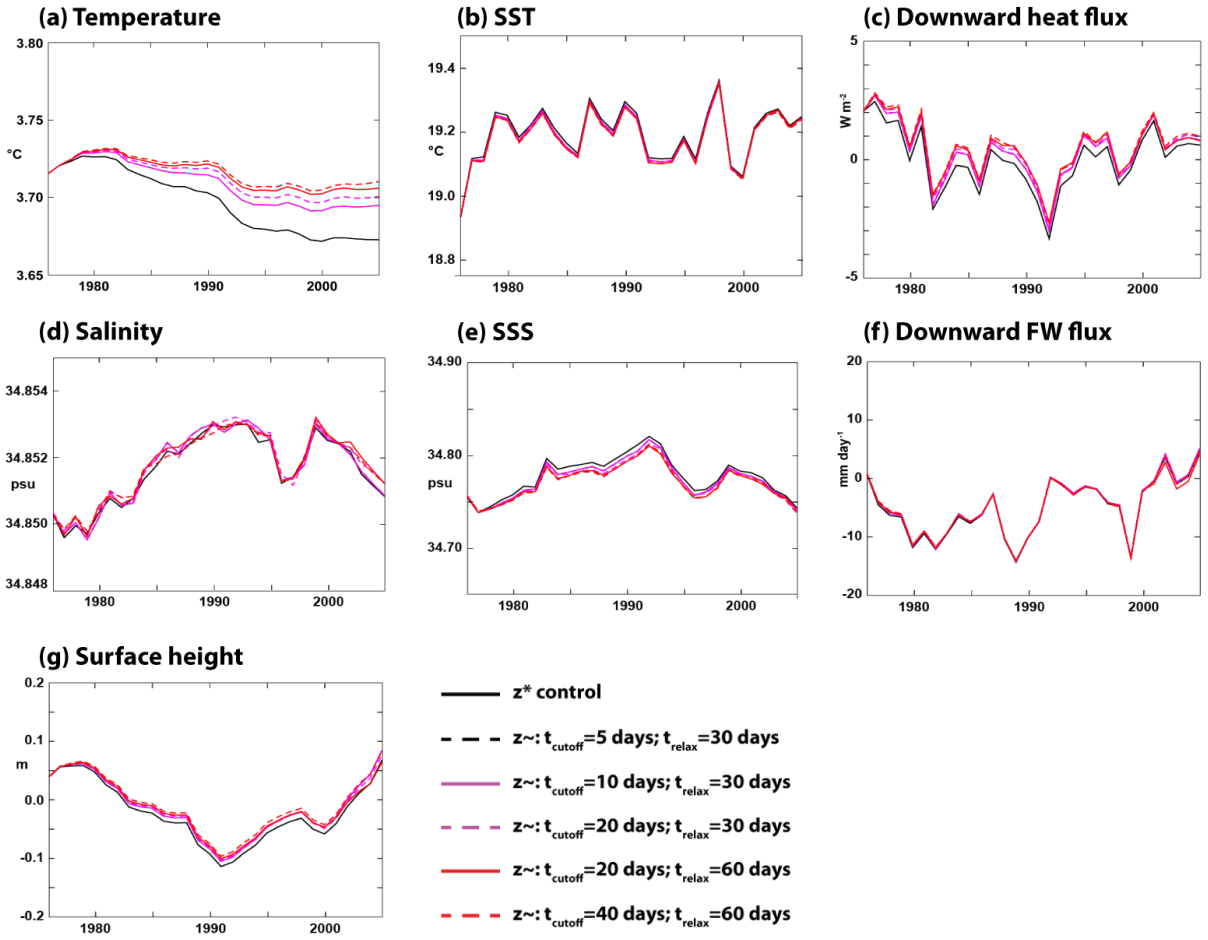

Figure 10: Global mean quantities as time series of annual means: (a) temperature in °C; (b) surface temperature in °C; (c) surface downward heat flux in W m^{-2}; (d) salinity in psu; (e) surface salinity in psu; (f) downward freshwater flux in mm day^{-1}; and (g) surface height in m.

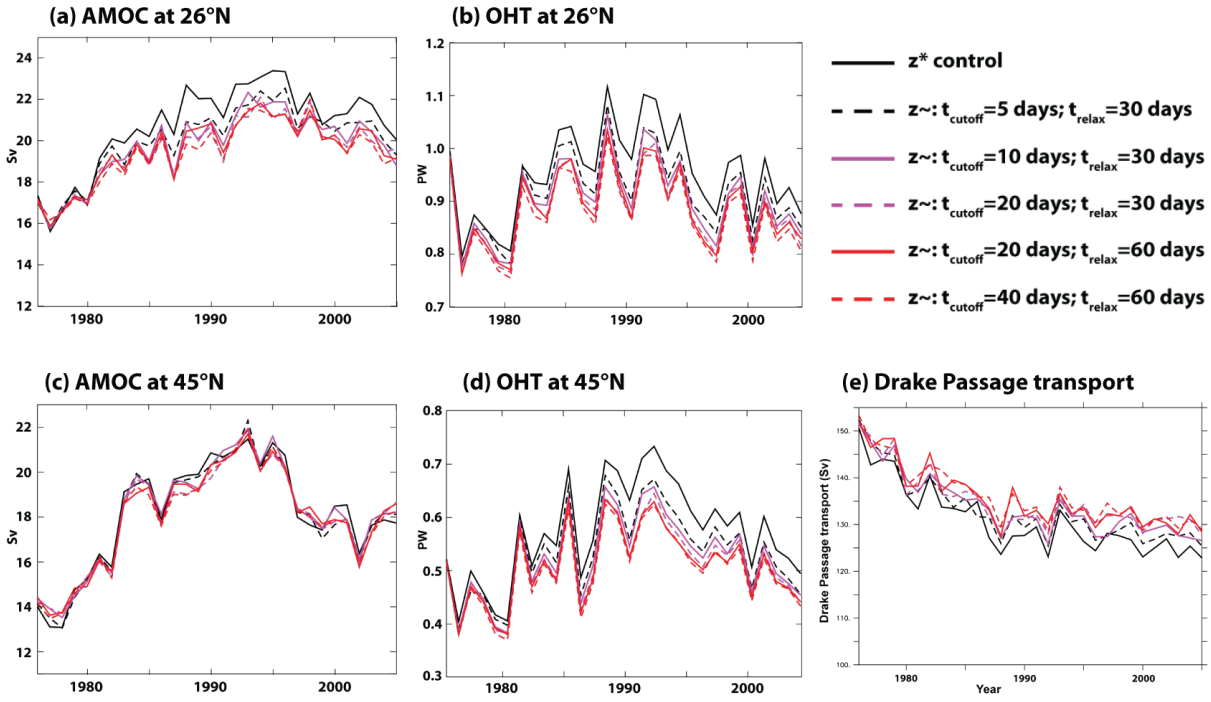

Figure 11: Large-scale transports in the model experiments: (a) AMOC strength in Sv at 26°N; (b) ocean meridional heat transport in PW at 26°N; (c) AMOC strength in Sv at 45°N; (d) ocean meridional heat transport in PW at 26°N; and (e) volume transport in Sv through Drake Passage.

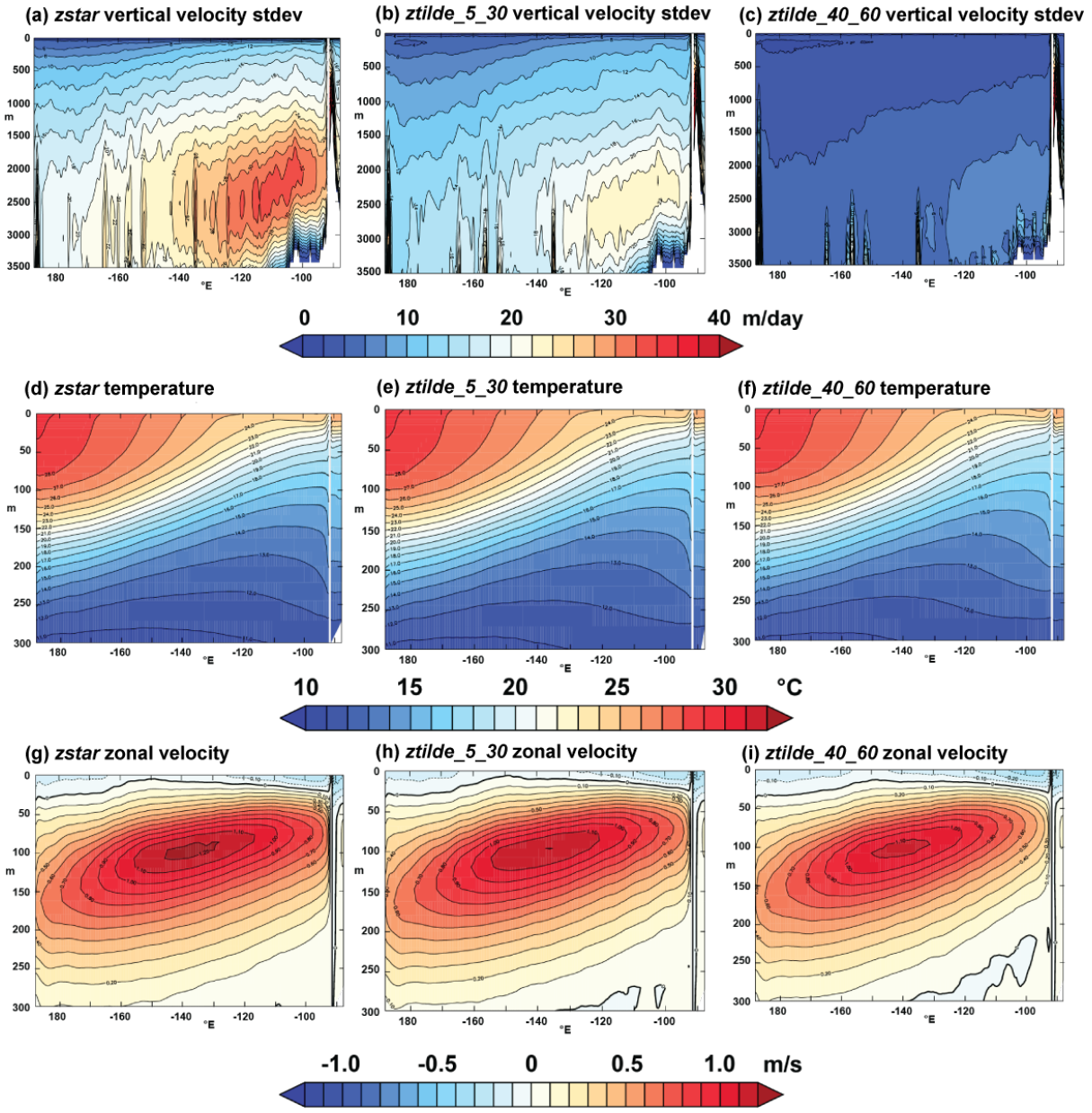

Figure 12. Standard deviation of vertical velocity in m day^{-1} on a section in the Equatorial Pacific in years 1996-2005 of (a) *zstar*; (b) in *ztilde_5_30*; and (c) in *ztilde_40_60*; upper ocean temperature on the Equator in (d) *zstar*; (e) in *ztilde_5_30*; and (f) in *ztilde_40_60*; and zonal velocity in m s^{-1} on the same section in (g) *zstar*; (h) in *ztilde_5_30*; and (i) in *ztilde_40_60*